CO_2 Capture and Reduction

Placing the process in an industrial framework

Jamie Hoetmer

TU Delft

CO_2 Capture and Reduction

placing the process in an industrial framework

by

Jamie Hoetmer

to obtain the degree of Master of Science

at the Delft University of Technology,

to be defended publicly on Wednesday June 29, 2022 at 2:00 PM.

Student number:	4629337	
Project duration:	August 18, 2021 – June 29, 2022	
Thesis committee:	Prof. dr. A. Urakawa,	TU Delft, supervisor
	Prof. dr. J.J.C. Geerlings,	TU Delft, supervisor
	Dr. A. Bansode,	TU Delft

An electronic version of this thesis is available at http://repository.tudelft.nl/.

Picture on the cover page is available at [1].

TU Delft

Abstract

Capturing and utilizing the emissions of CO_2 has become a method to reduce the occurring emissions from industrial flue gases. One of the methodologies to capture and use the CO_2 is through the CO_2 capture and reduction (CCR) process. This process uses a bi-functional catalyst to capture CO_2 from diluted gas streams and subsequently reduce it to CO in the presence of H_2. The obtained product (syngas) can be further used as feedstock in for example the Fischer-Tropsch process. To implement a novel technology in industry, the technology itself should be economical feasible.

To determine the feasibility of the process a techno-economical analysis is executed. The analysis uses process parameters obtained by evaluating the catalytic activity of the bi-functional catalysts. Two catalytic systems have been evaluated: Cu-K/γ-Al_2O_3 and FeCrCuK/PMG20. Effect on the synthesis conditions of Cu-K/γ-Al_2O_3 were also investigated. Cu-K/γ-Al_2O_3 without additional drying steps during the synthesis shows a higher CO_2 capacity and a faster CO production rate compared to the other catalysts. Furthermore, to estimate the H_2 requirement in an industrialized process the consumption of H_2 during the process has been quantified.

To ensure a continuous process operation, a two-reactor process has been proposed in the techno-economical analysis. The sizing and subsequent cost of the process equipment has been determined by utilizing the obtained process parameters. Besides the capital costs, the operating costs were also estimated to determine the profitability of the process. After the monetary benefit of selling the syngas was determined, it could be stated that the process is profitable under certain conditions. The process is profitable if the used H_2 source has a buying price below \$1.8 per kilogram. If sales of allowances is possible, the buying price of H_2 needs to be below \$2.4 to ensure a profitable process.

Acknowledgements

These last 10 months working on this project in the *Catalysis Engineering* group at *Delft University of Technology* have been a great learning opportunity. First of all, I would like to thank Donato Pinto for teaching me the ropes regarding the setup and the CO_2 capture and reduction concept.

Secondly, I would like to thank Prof. dr. Atsushi Urakawa and Prof. dr. Hans Geerlings for their support and input throughout the project. Furthermore, I would like to thank Dr. Atul Bansoda for taking the time in being part of my thesis defense committee. I would further like to recognise the help of Dr. Mahinder Ramdin for his help regarding the techno-economical analysis of my project.

I would like to thank the entire *Catalysis Engineering* group for welcoming me, especially the other students in office E2.380 for always being open to have a conversation.

Last but not least, I would like to thank my friends and family for their support throughout the project. A special mention goes to Sam for celebrating the highs and helping me through the lows these past 10 months.

Jamie Hoetmer
Delft, June 2022

Abbreviations

BET Branauer-Emmett-Teller

CAPEX Capital expenditure

CCR CO_2 capture and reduction

CCS Carbon capture and storage

CCU Carbon capture and utilization

EDS Energy dispersive X-ray spectroscopy

EU ETS European Union emission trading scheme

GHG Greenhouse gas

MS Mass spectrometer

OPEX Operational expenditure

PBP Payback period

PFD Process flow diagram

SEM Scanning electron microscopy

TGA Thermogravimetric analysis

XRD X-ray diffraction

Contents

List of Figures

List of Tables

1 Introduction

In the year 2021 the overall greenhouse gas emissions reached their highest level ever. The total greenhouse gas emissions reached 40.8 Gt of CO_2 equivalent, which are mostly caused by CO_2 emissions from energy combustion and industrial processes [2]. To limit the warming effect caused by greenhouse gasses, these CO_2 emissions need to be reduced. New technologies are in development to capture the emitted CO_2 and use or store it elsewhere. Currently, policies are in place to ensure a market incentive to reduce these emissions such as the EU emission trading scheme (ETS).

Important strategies that have been suggested to reduce the CO_2 emissions are the carbon capture and storage (CCS) and carbon capture and utilization (CCU) processes. In both of these strategies the CO_2 is captured and transported to the place of usage or storage. However, the CO_2 capture in both of these strategies represents a major fraction of the total costs, since the flue gas in post-combustion technologies contains low concentrations of CO_2. Due to these low concentrations in flue gas, chemical solvents are utilized as sorbents, and to regenerate these solvents a large energy penalty takes place. Furthermore, current utilization techniques require pure CO_2 streams. These concentrated streams can be converted into valuable products such as plastics, fuels and other chemicals.

In order to capture and utilize low concentrations of CO_2, the CO_2 capture and reduction (CCR) process can be used. In this process a bi-functional catalyst operates continuously under isothermal and unsteady-state conditions, to capture and reduce the CO_2. By employing H_2 as a reducing agent, the captured CO_2 is reduced to CO, the resulting product is synthesis gas (syngas). This syngas can be converted into chemical products to use in the existing energy infrastructure such as methanol. To utilize this process in industry, it should be researched whether this process is (economically) feasible. This leads to the main question this project aims to answer: *What is the economical feasibility of the CO_2 capture and reduction process for industrial applications?*

To answer this question a techno-economical analysis is executed. This analysis relies on experimental results obtained during the thesis and from previous research. The report has been structured to cover subjects related to the catalyst, as well as the techno-economical analysis. In Chapter 2 the background is presented, which includes CCU, CCS, possible H_2 production routes and information related to the European Union Emission Trading Scheme (EU ETS). Chapter 3 discusses the synthesis of the bi-functional catalysts and the used characterization methods. Furthermore, the reactor setup, a protocol for catalyst screening and a protocol to quantify the H_2 during the process are discussed. Chapter 3 ends with an explanation on the economical analysis used in this thesis. This chapter is followed by the characterization results of the bi-functional catalysts in Chapter 4. Chapter 5 discusses the results obtained regarding the reactor setup, the catalyst screening and the H_2 quantification. The techno-economical analysis is discussed in Chapter 6. In Chapter 7 the conclusions and recommendations are addressed.

2

Background

It is recognized that the observed global warming since the mid-20th century is mainly caused by human activity [3]. The energy required to satisfy the demand of the global economy is obtained through a variety of fuels such as oil, natural gas, and coal. The production of the fuels results in greenhouse gas (GHG) emissions of which CO_2 holds the highest share. Emissions from industry results in 30% of total GHG emissions [4]. An increase in the concentration of greenhouse gasses produces a warming effect, which has a detrimental impact on the livability of the planet due to increased temperatures and droughts. To mitigate global warming, a target is set by the members of the European Union to have net zero greenhouse gas emissions by 2050. To obtain the net zero emissions changes need to occur in the current energy infrastructure: directly capturing the CO_2 from the emitting sources in the industrial sector represents an opportunity with high potential to meet the proposed targets. Besides electrification and higher required efficiencies, the cost of emitting carbon needs to be raised. Carbon pricing is seen as an important tool for decarbonisation.

There are two main methods to set a carbon price, a carbon tax or an emissions trading system (ETS). The carbon tax is a carbon pricing at national level, while the ETS is on a European level. In this report the focus will be on the EU ETS. The EU ETS was established in 2005, and it covers the EU 27 as well as Iceland, Liechtenstein and Norway. The EU ETS has evolved over the years, and is currently in Phase 4 [5]. Phase 1 started in 2005 and ended in 2007. The purpose of the first phase was to put the system in place and let the participants familiarize themselves. Policy improvements and adaptations were undertaken before phase two started in 2008, and ended in 2012. In phase two, more greenhouse gasses were covered, and the proportion of free allocations were lowered. At the end of phase two the surplus of allowances became larger due to the economic crisis in 2008 which resulted into a lower demand for allowances [6]. Phase three started in 2013 and ran until 2020. Central policy changes occurred compared to the first two phases to raise the effectiveness of the system [6]. In the first two phases most allowances were given for free, but in phase three auctioning became the default method for allocation. Power generators do not receive any free allowances anymore, while airlines and the manufacturing industry still receive allowances for free [7]. To tackle the surplus of allowances following from the economic crisis, two main policy measures were implemented during phase three.

These two measures are the back-loading and the market stability reserve [8]. The back-loading was used as a postponement of the auctioning of allowances to re-balance the supply and demand in short term. For the long-term solution the market stability reserve was implemented in 2019 [8]. The market stability reserve is designed to absorb the surplus of allowance, and adjust the supply with respect to future uncertainties. So the market stability reserve soaks up the surplus of allowance that has built up over time, and releases it back into the market if the demand for allowances is greater than expected [8]. By placing the allowances in the market stability reserve, the clearing price for the allowances has increased in recent years [5]. In February 2022 the cost for an EU carbon permit became the highest in the EU ETS history at 97 euros per ton of CO_2 [9]. The past few months the average price of the EU carbon permit has been 80 euros per ton of CO_2 [9]. The fluctuation of the carbon price is visualized in Figure 2.1.

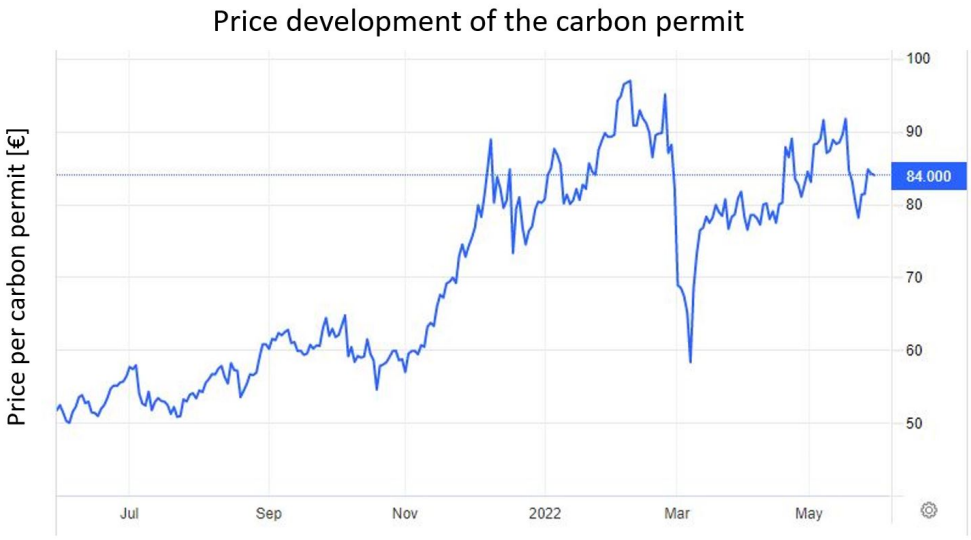

Figure 2.1: Development of the price for a carbon permit [9].

Currently, phase four is active and covers around 40% of the EU's GHG emissions [5]. The quantity of free allowances allocated to installations is dependent on the benchmark and whether the sector has a high risk of carbon leakage [7]. Manufacturing industries can still receive allowances as was the case in phase three. Sectors at a high risk of relocating their production outside of the EU will receive 100% of their allowances for free [7]. For sectors with a lower risk, free allocation will be phased out until no free allocations occur at the end of phase four. Sectors at a high risk of carbon leakage are for example manufacturing of petroleum products, cement, and oils and fats [7]. The allocation of allowances is based on the benchmark for that product, where the processes in the top 10% obtain all the required allowances [7].

2.1. Carbon Capture Utilization and Storage

To reduce the requirement for allowances, the CO_2 emissions of processes need to be reduced. To reduce the CO_2 emissions, the CO_2 can be captured and subsequently stored (CCS) or utilized (CCU). The difficulty in the capture of CO_2 is the concentration present in the flue gas from the processes. The majority of emission sources have CO_2 concentrations of less than 15% [10, 11, 12].

Numerous technological options exist that can be utilized to capture or purify the produced CO_2. Currently, three technological options are generally used. These are post-combustion CO_2 capture using amine solvents, calcium looping technologies, and oxyfuel combustion [13]. Post-combustion CO_2 capture is a technology that is an addition to an industrial process. The addition will not affect the operation of the facility the capture is attached to. The capture usually makes use of a chemisorption process with an amine solvent. The chemisorption process has considerable capital expenditure (CAPEX) and operational expenditure (OPEX) associated with its use. An increase of 40% to 80% of the CAPEX occurs when adding post-combustion capture to a process [12]. Furthermore, due to the low concentration of CO_2 in flue gas, large amounts of solvent are needed. The solvent needs to be regenerated for re-use bringing an additional energy penalty associated to that.

A second capture method is the use of a calcium looping technology, which utilizes high-temperature solid sorbents. Two reaction vessels are present in this technology. In one vessel a carbonation reaction occurs to react CO_2 to $CaCO_3$ [14]. In the second reaction vessel, $CaCO_3$ is heated to reverse the reaction and consequently releasing CO_2 [14]. Due to the high temperatures required for the capture and the release of CO_2, the process is not energy efficient [14].

The third capture method is using pure O_2 instead of air during the combustion of the feedstock [13]. This results in a flue gas that contains mostly CO_2, which is recycled from the reactor outlet. For this process, pure O_2 is needed. However, a O_2 separation plant is associated with a significant energy penalty [15].

The three previously discussed technologies are used to create a flow of CO_2 which can be processed further. Two pathways are possible for the captured CO_2: stored or used in a different application. Various approaches can be used to store the pure CO_2. One of these approaches is geological storage by injecting CO_2 into underground geological formations such as oil and gas fields. Another approach is storage of CO_2 in stable carbonates by reacting the CO_2 with metal oxides [13]. The CO_2 can be utilized in a multitude of pathways. Such pathways are the production of CO_2-based chemical products and fuels, and CO_2 enhanced oil recovery [13, 16].

For the storage and utilization of CO_2, highly concentrated CO_2 is required. The previously mentioned capture methods require a significant energy penalty [15]. Besides the capture of CO_2, the CO_2 needs to be transported to a different location for the storage or utilization. The objective is to design a process without a significant energy penalty and where CO_2 can immediately be utilized. One method is the post-combustion CO_2 capture and reduction process.

2.2. CO_2 Capture and Reduction Process

The CO_2 capture and reduction (CCR) process can increase the efficiency of the CO_2 capture and utilization by using a bi-functional catalyst. The capture and reduction occurs in subsequent steps resulting in an unsteady-state operation. In CCR two steps are present: the capture of CO_2 on the catalyst, followed by the catalytic reduction of the captured CO_2 by a reducing gas. The CCR process is operated under isothermal conditions and can operate under atmospheric pressure. High capture efficiencies are achieved as well as high activities and selectivities [12]. The advantage of the CCR process is that the diluted CO_2 can directly be converted into chemicals that can be used in other processes, such as syngas. In this thesis, H_2 is employed to reduce CO_2 to CO. The product composition is subsequently a mixture of CO and H_2, in the remainder of the report denoted as syngas.

The process utilizes a bi-functional catalyst to ensure the capture and reduction of CO_2. The bi-functional catalyst consists of a variety of metals impregnated on a support. The catalyst should satisfy a few requirements such as a high CO_2 capacity, and fast CO_2 reduction [12]. Furthermore, a selective reduction should occur and the catalyst should consist of abundant chemical elements and materials.

Based on previous research and the mentioned requirements, two different catalyst compositions are tested in this thesis. The first bi-functional catalyst was developed by Hyakutake et al., consisting of K and Cu deposited on a γ-Al_2O_3 support [17]. The support has a high mechanical strength, high surface area, and is quite inexpensive to produce [18]. The potassium present in the catalyst is used to enable high CO_2 capture efficiency, while Cu is required for the CO_2 reduction. Hyakutake et al. show that when using Cu-K/γ-Al_2O_3, an efficient process is obtained, as almost all of the CO_2 is captured and reduced [17]. Furthermore, a high selectivity to CO during the reduction phase is observed, which is beneficial for the further processing of the syngas [17].

The second catalyst utilized in this project was developed by Bobadilla et al. [12]. A large variety of active catalysts were screened and optimized. The bi-functional catalyst that showed promising CO_2 capture and subsequent reduction into CO is a catalyst that contains Fe, Cr, Cu, and K supported on a hydrotalcite. The hydrotalcite material is a mixture of Mg and Al oxides. The Cr is present as a structural promoter that helps the iron from sintering at high temperatures [19]. A high stability of this catalyst was found for catalytic tests for ca. 45 h. Furthermore, full CO_2 capture was achieved, and subsequent reduction to CO accompanied by release of CO_2 [12]. Besides ideal gas compositions, Bobadilla et al. have performed experiments with the inclusion of O_2 and H_2O. The capture efficiency remained high (>90%) for all conditions, however, the CO_2 conversion was lowered in the presence of O_2 and H_2O [12]. It is speculated that their presence influences the state of active sites.

In order to fairly compare the performance of the two catalyst compositions, both are synthesized during this thesis and tested on their catalytic activity. The catalytic activity tests are executed using the same reactor setup and procedure. The objective is to select the best performing catalyst for the techno-economical analysis, based on the obtained CO_2 capture capacity and reduction rate.

Product Utilization

The products obtained from the CCR process can be directly utilized in industry, as long as the product composition is suitable for further processing. Syngas is employed in a variety of operations. The products obtained from these processes can be used as a carbon neutral source of energy, if no other emissions occur during the production. Figure 2.2 highlights the use of syngas as a feedstock.

Two processes will be shortly discussed: the Fischer-Tropsch synthesis and methanol production. The Fischer-Tropsch synthesis is a process that produces clean hydrocarbon fuels making use of a catalyst. Generally speaking, two forms of industrially generated Fischer-Tropsch synthesis exist. The first one is a high-temperature Fischer-Tropsch synthesis using an Fe-based catalyst operating at minimal temperatures of 320 °C [20]. The second one occurs at lower temperatures (170-270°C), primarily using an Fe- or Co-based catalyst [20]. Depending on the temperature and the used catalyst, a H_2/CO ratio between 0.5-2.5 is used [20].

Another application that makes use of syngas is the methanol synthesis. Methanol can be further used as a feedstock to produce chemicals such as gasoline and olefins (Figure 2.2). The majority of methanol synthesis is based on syngas obtained from natural gas or coal [21]. However, it is possible to use the converted CO_2 from the CCR process as the feedstock. To obtain full conversion into methanol, a H_2/CO ratio of 2 is required.

Based on these processes that use syngas as a feedstock, the product composition of the CCR process is aimed at a H_2/CO ratio of 2.

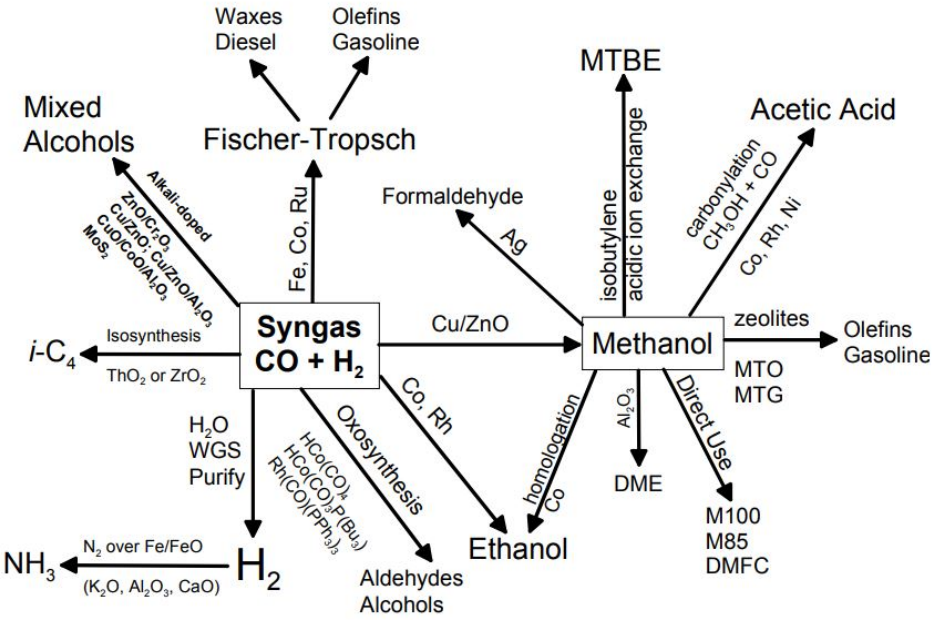

Figure 2.2: Example of syngas and methanol uses [22].

2.3. Hydrogen Production

As mentioned previously, a flow of H_2 is used to reduce the CO_2 into CO. Current commercial production methods of H_2 make use of fossil fuels, water or biomass as resources. The use of fossil fuels accounts for 95% of the production, and electrolysis produces around 5% [23]. To differentiate the production routes of H_2, a color code is commonly used. In this thesis three shades of H_2 are discussed; grey, blue and green H_2.

From these three, the most polluting variant is grey H_2. In this production method, fossil fuels are used as feedstock. An example of grey H_2 is the production via steam methane reforming. The fossil fuels react with water to produce H_2 and CO (Reaction R2.1).

$$CH_4 + H_2O \leftrightarrow CO + 3\,H_2 \tag{R2.1}$$

Furthermore, a water-gas shift reaction (Reaction R2.2) is performed after the reforming to obtain more H_2. The production of H_2 through this pathway results in substantial CO_2 emissions, roughly 9.3 kilograms CO_2 per kg H_2 [24].

$$CO + H_2O \leftrightarrow CO_2 + H_2 \tag{R2.2}$$

If the CO_2 from the production processes is captured, the production method is denoted as blue H_2. Blue H_2 is grey H_2 with carbon capture and storage attached to the process. By making use of CCS, the current installations can be utilized with lower GHG emissions. Unfortunately, the current CCS capture efficiencies are 85-95% [23]. This means that significant CO_2 emissions still occur while utilizing blue H_2. Blue H_2 can reduce the occurring CO_2 emissions, but it can only be seen as a short-term solution before another source of H_2 is implemented for the sustainable energy transition.

The most suitable H_2 for this transition is green H_2. This is a production method of H_2 without occurring GHG emissions. Currently, the most established technology for the production of green H_2 is water electrolysis. This water electrolysis can be fuelled by renewable electricity. More H_2 production methods using renewable energy exist such as thermochemical water splitting, photolysis and combined photoelectrochemical water splitting [25]. A schematic of the different shades of H_2 production is found in Figure 2.3.

Currently, there are barriers that prevent the contribution of (green) H_2 to the energy transition. The barriers that apply to all the shades of H_2 are for example lack of transport and storage infrastructure. Furthermore, there are barriers related to the production of green H_2. These are for example the high production costs and energy losses during the electrolysis. Furthermore, green H_2 should only utilize renewable electricity for the production. However, if an electrolyser is attached to the grid, it is possible that electricity produced from fossil fuel plants is supplied. If this is the case, the sustainability of the H_2 can not be ensured.

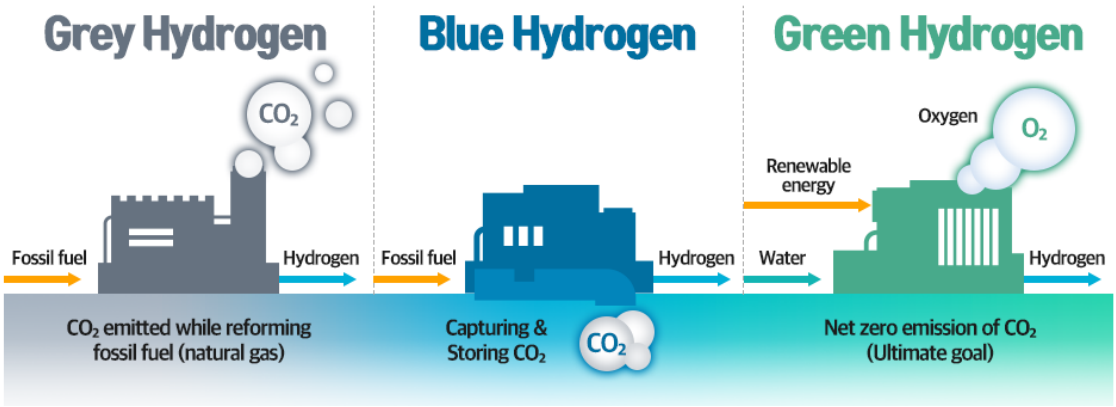

Figure 2.3: Grey, blue and green H_2 production methods [26].

3 Methodology

In this chapter the methodology of the research is discussed. Firstly, the synthesis of the catalysts as well as the used materials are discussed in Section 3.1. After that, the used characterization techniques are described. This is followed by a description on the reactor setup and the procedure used for the activity experiments (Section 3.3). In Section 3.4 and 3.5 the protocols for catalyst screening and H_2 quantification are discussed, respectively. The chapter is finalized with a section regarding the economical analysis used in the techno-economical analysis.

3.1. Catalyst Preparation

During this research two catalysts compositions are used. The synthesis of the catalyst with Cu and K is described in Section 3.1.1. The synthesis of the catalyst with Fe, Cr, Cu, and K is described in Section 3.1.2. The chemicals used for the synthesis and their supplier are mentioned in Table 3.1.

Table 3.1: Materials used in catalyst synthesis.

Chemical	Formula	Supplier	CAS-number
Aluminium oxide (γ-phase)	γ-Al_2O_3	Alfa Aesar	215-691-6
Copper (II) nitrate trihydrate	$Cu(NO_3)_2 \cdot 3\,H_2O$	Merck KGaA	10031-43-3
Potassium carbonate	K_2CO_3	Sigma-Aldrich	5845-08-07
Iron (III) nitrate nonahydrate	$Fe(NO_3)_3 \cdot 9\,H_2O$	Honeywell	7782-61-8
Chromium (III) nitrate nonahydrate	$Cr(NO_3)_3 \cdot 9\,H_2O$	Sigma-Aldrich	7789-02-8
Aluminum magnesium hydroxy carbonate	PMG20	Sasol Germany GmbH	595-02-0

3.1.1. Cu-K/Al_2O_3

Two different methodologies were used to produce the catalyst containing copper and potassium. The main difference between the two catalysts is the additional drying steps present in one of the synthesis methodologies. Firstly, the catalyst without additional drying will be discussed (type 1). Secondly, the catalyst with the addition drying will be discussed (type 2). The target composition of both of the catalysts is 11 wt% Cu, 10 wt% K and 79 wt% γ-aluminium oxide (γ-Al_2O_3).

Cu-K/γ-Al_2O_3 Type 1

During the synthesis the metals are impregnated on γ-Al_2O_3 in subsequent steps. Firstly, Cu is impregnated, followed by the impregnation of K. To prepare the support for the incipient wetness impregnation, the γ-Al_2O_3 pellets are crushed into a fine powder. This fine powder is weighed to obtain the target composition. To obtain 10 wt% of Cu in the synthesised catalyst, a precursor solution of $Cu(NO_3)_2{\cdot}3\,H_2O_{(aq)}$ with Milli-Q water is prepared. For the incipient wetness impregnation method the amount of Milli-Q water added is consistent with the pore volume of γ-Al_2O_3. Data provided by *Alfa Aesar* shows that the pore volume of the used γ-Al_2O_3 is 1 $cm^3\,g^{-1}$. So per gram of support, 1 $cm^3\,g^{-1}$ of Milli-Q is used in the synthesis.

The precursor solution is pipetted over the crushed γ-Al_2O_3 support and mixed into a homogeneous paste, using a mortar and pestle. This impregnates the support due to capillary forces. This paste is dried overnight in an oven at 80 °C, followed by a calcination at 500 °C for five hours to remove impurities and volatile matter. A heating rate of 10 °C/min is used.

After calcination the powder is grounded, and weighed to determine the required mass of K. To determine this mass it is assumed that all Cu is oxidized to CuO. The required amount of K_2CO_3 is weighed and dissolved in Milli-Q before impregnation. The amount of Milli-Q is based on the pore volume of 11Cu/γ-Al_2O_3, using N_2 adsorption it is determined that the pore volume is 0.62 $cm^3\,g^{-1}$. The dissolved K_2CO_3 is pipetted over the ground 11Cu/γ-Al_2O_3 and mixed into a homogeneous paste using a mortar and pestle. After impregnation of the Cu/γ-Al_2O_3 with K_2CO_3 the catalyst is dried and calcined using the procedure mentioned previously.

The powder obtained from the synthesis is ground into a fine powder and pelletised at 4 tons for one minute. These pellets are crushed and sieved to obtain a powder within the range of 200 - 300 µm. This results in a catalyst which will be denoted as Cu-K/γ-Al_2O_3 type 1 for the remainder of the report.

Cu-K/γ-Al_2O_3 Type 2

According to previous research pre-drying of the Cu/γ-Al_2O_3 intermediate can result into a higher catalytic performance [27]. This could occur due to more accessible pores for the precursors after drying. Considering this result, a second Cu-K/γ-Al_2O_3 catalyst is fabricated using more pre-drying steps and impregnation in a controlled environment.

To compare the two different methodologies, the same composition is pursued: 11 wt% Cu, 10 wt% K and the remainder /γ-Al_2O_3. The first step in the synthesis is equal to the Cu-K/γ-Al_2O_3 type 1 catalyst: crushing of γ-Al_2O_3 pellets. The fine powder is weighted to obtain a composition of 79 wt% of the final catalyst weight. This fine powder is transferred into a glass vial and placed inside an oven at 150 °C overnight. After the pre-drying of the support, the vial is taken out of the oven and the cap is screwed onto the vial to limit the adsorption of water.

A weight loss of 12.8% occurs during the pre-drying of the support [27]. The amount of $Cu(NO_3)_2{\cdot}3\,H_2O_{(aq)}$ needed to obtain the proper composition is weighed. This amount of $Cu(NO_3)_2{\cdot}3\,H_2O_{(aq)}$ is diluted in Milli-Q as in the previous methodology. This means that per gram of γ-Al_2O_3 1 $cm^3\,g^{-1}$ of Milli-Q is used to dissolve the precursor. The closed vial with the γ-Al_2O_3 is placed inside a glovebox as shown in Figure 3.1. Within this inert environment the γ-Al_2O_3 is deposited into a mortar and pestle. This is subsequently sealed off with different layers of parafilm. The mortar is sealed off to obtain an inert environment during the impregnation. After the γ-Al_2O_3 is inside of sealed mortar, it is taken out of the glovebox and put inside a fume hood. To maintain the inert environment inside the mortar, the $Cu(NO_3)_2{\cdot}3\,H_2O_{(aq)}$ is injected through the layers of parafilm with an injection needle. This is mixed till a homogeneuous paste is obtained, after which the injection needle and the parafilm are removed. After this mixing, the mortar is put into the oven at 80 °C overnight. After drying, Cu/γ-Al_2O_3 is grounded into a powder and calcined at 500 °C for five hours to remove impurities and volatile matter.

Figure 3.1: Glovebox used for the production of Cu-K/γ-Al_2O_3 type 2.

After drying and calcination, the synthesized Cu/γ-Al_2O_3 is transferred to a glass vial. This vial is placed in an oven at 150 °C overnight. After the pre-drying the vial with Cu/γ-Al_2O_3 is sealed inside the oven, taken out of the oven and then placed inside the glovebox. The Cu/γ-Al_2O_3 is transferred to a mortar and pestle inside the inert glovebox. These are again sealed off with parafilm to contain the inert atmosphere. In a fumehood the K_2CO_3 solution is prepared by dissolving the proper amount in Milli-Q. After the solution is prepared, the mortar sealed with parafilm with the Cu/γ-Al_2O_3 is taken out of the inert glovebox. The K_2CO_3 solution is injected through the parafilm layers, followed by mixing to obtain a homogeneous paste. The parafilm is removed after

this paste has reached a homogeneous consistency. The mortar is placed into an oven at 80 °C overnight, followed by calcination at 500 °C for five hours.

The powder obtained from the synthesis is ground into a fine powder and pelletised at 4 tons for one minute. These pellets were crushed and sieved to obtain a powder within the range of 200 - 300 µm. This results in the Cu-K/γ-Al_2O_3 type 2 catalyst used in the remainder of the report.

3.1.2. FeCrCuK/PMG20

The other type of catalyst that is synthesised is a hydrotalcite supported FeCrCu-K catalyst, the methodology is obtained from Bobadilla et al. [12]. The used hydrotalcite consists of magnesium and aluminium, with a MgO content of 20 wt%. The type of support with this composition is denoted as PMG20.

The catalyst has a target composition of 80 wt% PMG20, 10 wt% K, 8.8 wt% Fe, 1 wt% Cr and 0.2 wt% Cu. The catalyst is prepared using a sequential impregnation using the incipient wetness impregnation method. To obtain the homogeneuous mixed oxides required for the impregnation, PMG20 undergoes a thermal treatment at 600 °C for three hours. After this thermal treatment, the first precursors are impregnated. During this first impregnation the metals, except potassium, are impregnated. For this $Fe(NO_3)_3{\cdot}9\,H_2O$, $Cr(NO_3)_3{\cdot}9\,H_2O$, and $Cu(NO_3)_3{\cdot}9\,H_2O$ are dissolved in Milli-Q. The amount of Milli-Q is based on the pore volume of the support. According to N_2 adsorption the pore volume of PMG20 is 0.55 $cm^3\,g^{-1}$. The solution is pipetted over the support and mixed into a homogeneuous paste using a mortar and pestle. This paste is dried in the mortar and pestle overnight at 80 °C. This is followed by calcination at 500 °C for five hours utilizing a heating rate of 10 °C/min.

Figure 3.2: The synthesized FeCrCuK/PMG20 catalyst before sieving.

After the calcination the powder is ground and the second precursor is impregnated. To obtain the potassium in the catalyst, a K_2CO_3 solution is prepared by adding Milli-Q to the metal. The dissolved K_2CO_3 is added to the previously obtained powder in a mortar and pestle and mixed till homogeneous. After mixing, the powder is dried overnight at 80 °C, followed by calcination at 500 °C.

The powder obtained from the synthesis is ground into a fine powder and pelletised at 4 tons for one minute. These pellets were crushed and sieved to obtain a powder within the range of 200 - 300 µm. This results in the FeCrCuK/PMG20 catalyst used in the remainder of the report.

3.2. Characterization Methods

This section discusses the used characterization methods for the catalyst. These characterization methods are X-ray diffraction (XRD), scanning electron microsopy (SEM) & energy-dispersive X-ray spectroscopy (EDS), and N_2 adsorption.

3.2.1. X-Ray Diffraction

To analyze the structure of crystalline materials, XRD measurements are performed. The measurements are performed on a '*Bruker D8 Advanced diffractrometer*'. The catalyst is ground into a fine powder and loaded on a sample holder. The diffractometer has a Cu – Kα source with a wavelength of 1.540 60 Å ($K\alpha_1$) and 1.544 39 Å ($K\alpha_2$). For the experiments a measurement time of 40 minutes was used in order to maximize the signal-to-noise ratio. The 2θ range during the experiments was from 10° to 90° in a theta-theta geometry. A motorised varied-divergent slit was used of 3 mm to keep the diffracted surface constant. The obtained diffractrograms were analyzes with the help of the DIFFRAC.EVA software. The settings are summarized in Table 3.2.

Table 3.2: Settings used during XRD characterization.

Scan Time	Range	Increment	Window	Rotation
40 minutes	10° - 90°	0.02	Fixed 3 mm	No rotation

3.2.2. Scanning Electron Microscopy and Energy-Dispersive X-Ray Spectroscopy

To evaluate the morphology of the catalysts, scanning electron microscopy (SEM) images as well as the energy dispersive X-ray spectroscopy (EDS) images were taken on a '*SEM Hitachi S4800*'. The sample is secured on a sample holder using carbon tape and inserted into the sealed chamber which is brought to a vacuum. To fabricate an image, a beam of electrons is focused on the sample. These electrons hit the surface and are rebound, these rebounded electrons are registered by a detector. This detector turns these rebounded electrons into an image.

The beam of electrons can also excite electrons present in the ground state, ejecting it from its shell. When the created electron hole is filled by another electron from an outer, higher-energy shell, the difference in energy may be released in the form of an X-ray. The number and energy of the X-rays emitted are measured by EDS. Since the difference in energy between shells is a characteristic of the atomic structure of the element, EDS can measure the elemental composition of the sample. For the EDS measurements a back-scattered electron image is used with a magnification of 1000x. Using this magnification yields an overall composition of that part of the catalyst.

3.2.3. N_2 Adsorption - Brunauer-Emmett-Teller Surface Area and Pore Volume

To determine the specific surface area of the sample the Brunauer-Emmett-Teller (BET) analysis is used. The surface area of the catalyst is of great importance in heterogeneous catalysis, since the reaction mostly occurs on the catalyst surface. By collecting physisorption isotherm data from the catalyst the BET method is applied to explain the adsorption of gas molecules on a solid surface.

To determine the previously mentioned physisorption isotherm the used instrument (Micromeritics TriStar II 3020) makes use of a static determination method. The samples are first degassed in N_2 for 15 hours at 150° to remove the adsorbed water. After degassing, the static determination method is used, which means that known amounts of nitrogen (N_2) are released into the sample cell. The sample cell is maintained at a constant temperature (77K) during the adsorption measurements. Due to the occurring adsorption the pressure in the confided volume changes. These volume changes are measured and utilized to generate the adsorption isotherm of the sample. After the saturation pressure has been reached and the adsorption layers are formed, the sample is removed from the nitrogen atmosphere and heated. As a result of this the adsorbed nitrogen is released from the sample and the amount of released nitrogen can also be quantified. The step-by-step generated information can be displayed as the physisorption isotherm in which the amount adsorbed ($\mathrm{mol\,g^{-1}}$) is plotted against the equilibrium relative pressure (p/p^0). The saturation pressure (p^0) is measured during the experiment. After the physisorption isotherm is obtained this can be transformed into the 'BET plot', from which the BET monolayer capacity is determined. The monolayer capacity is obtained due to the linear relation between the two axis of the 'BET plot'. After the monolayer capacity is known the BET specific area of the adsorbent can be calculated.

Besides the BET specific area, the pore volume of the samples can also be determined. The pore volume is estimated by converting the amount adsorbed at an equilibrium relative pressure of 0.99 to a liquid volume. The value is taken at this ratio since the pores are completely filled with nitrogen just before the saturation pressure.

3.3. Reactor Setup and Procedure

To test the capture and reduction capacity of the bi-functional catalysts a reactor setup is used. In this section the reactor setup and used experimental procedure is explained.

3.3.1. Reactor Setup

The catalytic activity tests are performed in a fixed bed reactor. The sieved catalyst is inserted in a quartz tube with an inner diameter and thickness of 4 mm and 1 mm respectively. Quartz wool is used to pack the catalyst in position, as visualized in Figure 3.3. In most experiments 200 mg of catalyst is used, resulting in a catalyst bed of roughly 2 cm long.

After inserting and packing the catalyst bed, a metal jacket is put around the reactor tube. The metal jacket ensures a homogeneuous heat distribution along the catalyst bed. The temperature of the reactor is measured by a thermocouple inserted into the reactor. The heating system consists of a heating box and a PID system to control the amount of power used to heat up the coil surrounding the metal jacket.

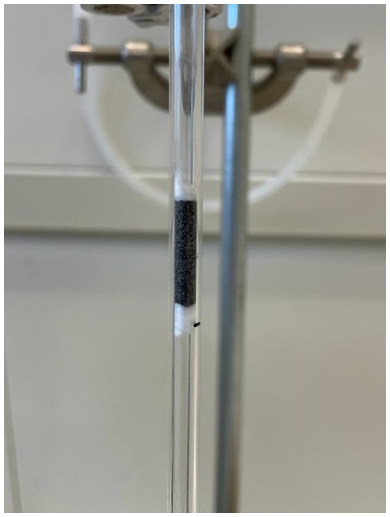

Figure 3.3: Catalyst tube with quartz wool to pack the catalyst in position.

A multitude of gasses are connected to the system, these are He, O_2, N_2, CO_2, CO, and H_2. The CO_2 and CO can be diluted using He, while the H_2 can be diluted using N_2. A system of two automatic 4-way switching valves are used to obtain the aimed inflow. Depending on the orientation of the four way valves, the flow goes through the reactor or goes to the vent. The orientation of the four way valves and the gas flow is controlled by a computer program called Labview. This program ensures automatic operation during the experiments. The outflow gas is analysed using a FT-IR spectrometer (Bruker-Alpha), with a time resolution of 5 seconds per spectra. Before every experiment a baseline is taken and subtracted from the obtained spectra. The outflow gas can also be analyzed using a mass spectrometry (MS).

Figure 3.4 shows the flowsheet of the reactor setup.

3.3.2. Experimental Procedure

Each catalytic activity experiment is split up in two distinct parts; the pre-treatment and the reaction step. In the pre-treatment step, the catalyst bed is heated up in a mixture of He and O_2. O_2 is used to remove any organic impurities. After the system has been heated up till 450 °C, the gas is switched to H_2 (50 mL min^{-1}) to reduce the catalyst. After an hour long reduction in H_2 the pre-treatment step is completed and the reaction step can occur.

In the reaction step switching takes place between the capture and reduction phase. During the capture phase CO_2 flows through the reactor, and during the reduction phase H_2 flows through. These flows can be diluted depending on the objective of the experiment. To have a clear distinction between the phases a He-flush is used between the two phases. Figure 3.5 shows a visualization of the experimental steps.

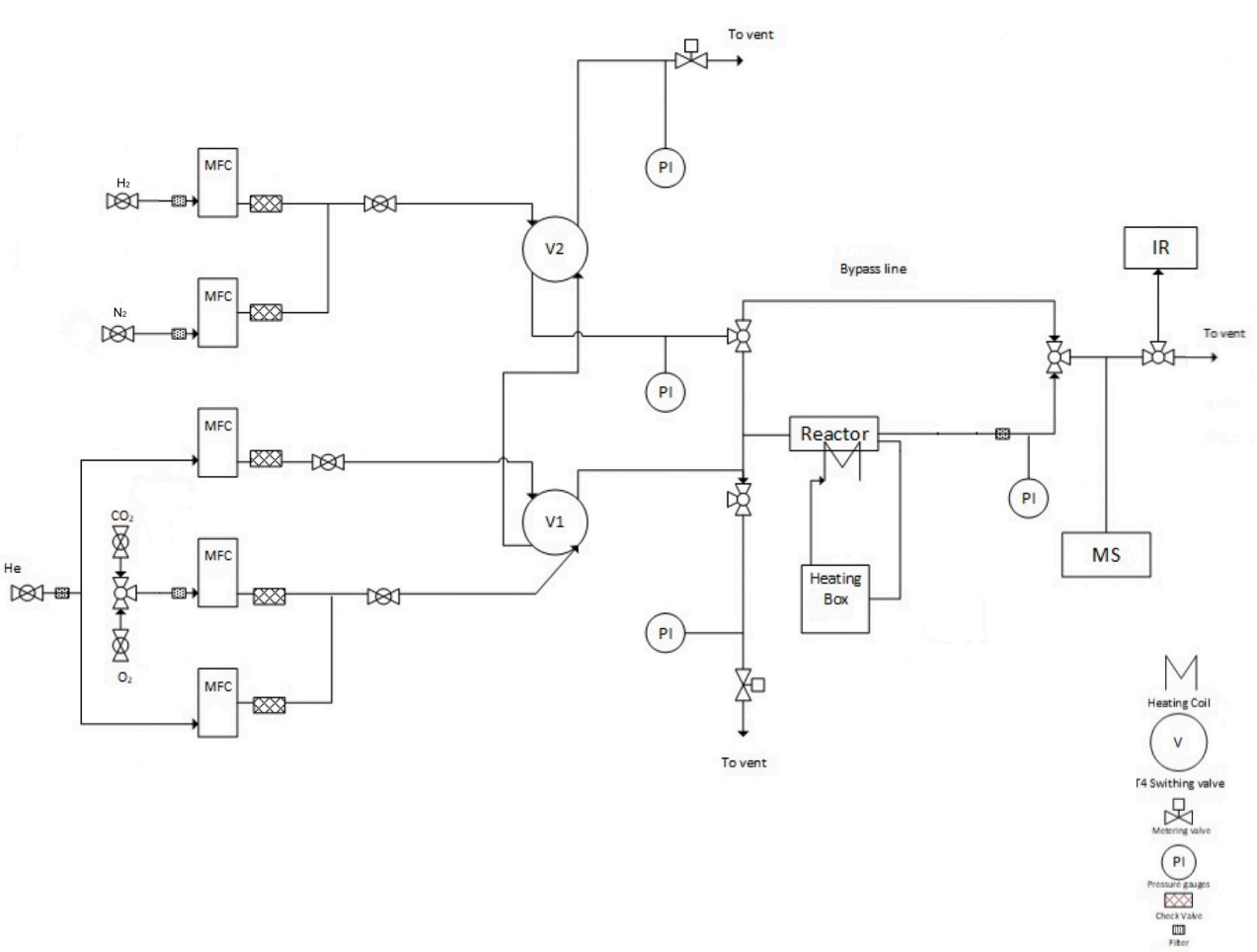

Figure 3.4: Flowsheet of the reactor setup.

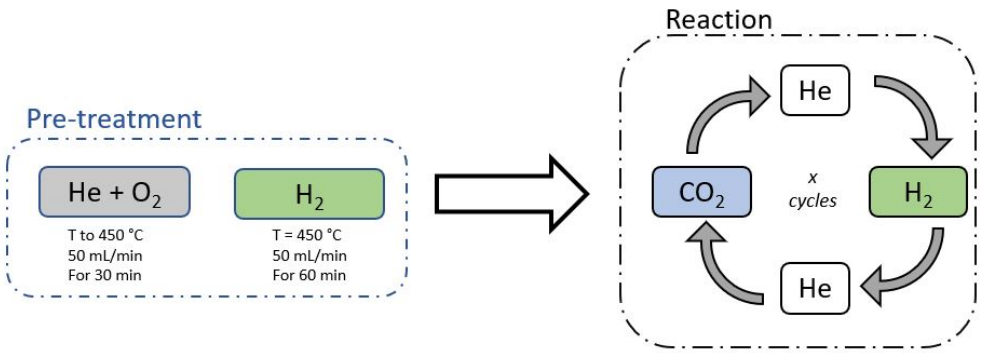

Figure 3.5: A schematic visualization of the experimental procedure.

The duration of the capture, reduction and flush phase is specified for each experiment. This duration corresponds to an amount of spectra taken by the FT-IR spectrometer. An equal duration of the capture and reduction phase is chosen during this project. Each experimental measurement consists of a blank measurement and an experiment. The blank measurement occurs at room temperature with the same flow rates, gas compositions and phase duration as the experiment. The blank measurement is used to analyze how the system behaves when no capture and reduction is taking place. This means that the difference in signal between the blank measurement and the experiment is caused by the capture and reduction of CO_2.

The blank measurement consists of three cycles of which the average is taken of the last two cycles. The experiment consists of six cycles of which the average of the last five cycles is taken. The first cycle is not taken into account due to the longer reduction in H_2 compared to the other cycles. This results in catalytic behaviour that does not represent regular operation.

From the experimental results a variety of parameters are obtained such as the CO_2 capacity of the catalyst. In this report the CO_2 capacity is determined as the amount of CO and CO_2 that flows out of the reactor during the reduction phase. The equation used to determine the CO_2 capacity is:

$$\text{CO}_2 \text{ capacity } [\text{mol g}^{-1}] = \frac{1}{W} \int_{t_{H_2,in}}^{t_{H_2,out}} [\dot{n}_{CO,out,exp}(t) + \dot{n}_{CO_2,out,exp}(t)]\, dt \tag{3.1}$$

where W, $t_{H_2,in}$, $t_{H_2,out}$, $\dot{n}_{CO,out,exp}$ and $\dot{n}_{CO_2,out,exp}$ are the catalyst weight, time of starting and ending the H_2 supply, and the molar flow rates of CO and CO_2 during the experiment, respectively.

As mentioned in Section 2.2, one of the requirements for the catalyst is a quick reduction of CO_2. To analyze the reduction rate of CO_2, the CO production rate is used:

$$\text{CO production rate } [\text{mol g}^{-1}\,\text{s}^{-1}] = \frac{\int_{t_{H_2,in}}^{t_{H_2,out}} [\dot{n}_{CO,out}(t)]dt}{(t_{H_2,out} - t_{H_2,in})W} \tag{3.2}$$

Furthermore, to specify the H_2 consumption during the catalytic tests, the amount of CO_2 captured during the capture phase needs to be determined. The following equation is used in this thesis:

$$\text{CO}_2 \text{ capture [mL]} = \int_{t_{CO_2,in}}^{t_{CO_2,out}} F_{CO_2,out,blank}(t)dt - \int_{t_{CO_2,in}}^{t_{CO_2,out}} F_{CO_2,out,exp}(t)dt \tag{3.3}$$

where $t_{CO_2,in}$, $t_{CO_2,out}$, $F_{CO_2,out,blank}$ and $F_{CO_2,out,exp}$ are the time of starting and ending the CO_2 supply, and the mass flow rates of CO_2 during blank and during the experiment, respectively.

3.4. Protocol for Catalyst Screening

In this project, two catalyst compositions are tested. However, a large variety of materials can be used during the production of the catalyst. This means a large range of catalysts can potentially be synthesised and used as a bi-functional catalyst in the CCR process. A catalyst should be able to capture the CO_2, and subsequently reduce the CO_2. The amount of CO_2 the catalyst can capture is important, without capture no reduction can take place. To quickly test the capture capacity, a methodology is developed. The hypothesis is that a thermogravimetric analysis (TGA) can be utilized for the catalyst screening. The METTLER TOLEDO SF/1100 is used for the analysis of the samples. The sample is loaded into a crucible and loaded into the machine. The flow of the gasses used in the experiments is 100 mL min^{-1}. The concentration for CO_2 and H_2 are 100 % and 5 % respectively.

The experiment for catalyst screening is executed with two different sets of inflow gasses. In one experiment, CO_2 and H_2 are alternated, in the other CO_2 and N_2 are alternated. During the utilization of H_2, the H_2 can interact with the sample to make CO_2 capture possible. This does not occur during the N_2 experiment. This means that the difference in weight change between the N_2 and H_2 experiment can correspond to the weight change caused by the capture of CO_2.

To determine the weight change caused by the gasses, the system is flushed for 10 minutes at room temperature. This is done with either H_2 or N_2, depending on the experiment. After this flush phase, the temperature is increased to 450 °C using a ramp of 10 °C min^{-1} under a H_2 or N_2 flow. After the temperature has been increased to 450 °C an hour long flow of H_2 or N_2 is supplied. A temperature of 450 °C is used due to its correspondence to the experiments performed in the reactor setup. After the hour long flow, the supplied gas is changed to CO_2 for 15 minutes, followed by a H_2 or N_2 flow for 15 minutes. The switching of the gas mimics the switching of the gas that takes place in the reactor setup. The weight change due to the presence of CO_2 is determined from the last three cycles of CO_2 flow. The weight change is determined by calculating the difference in weight before and after the CO_2 flow. The hypothesis is that the difference between the weight change in switching CO_2/N_2 and CO_2/H_2 corresponds to the capture of CO_2. A schematic overview of the experimental procedure for the quick catalyst screening is found in Figure 3.6.

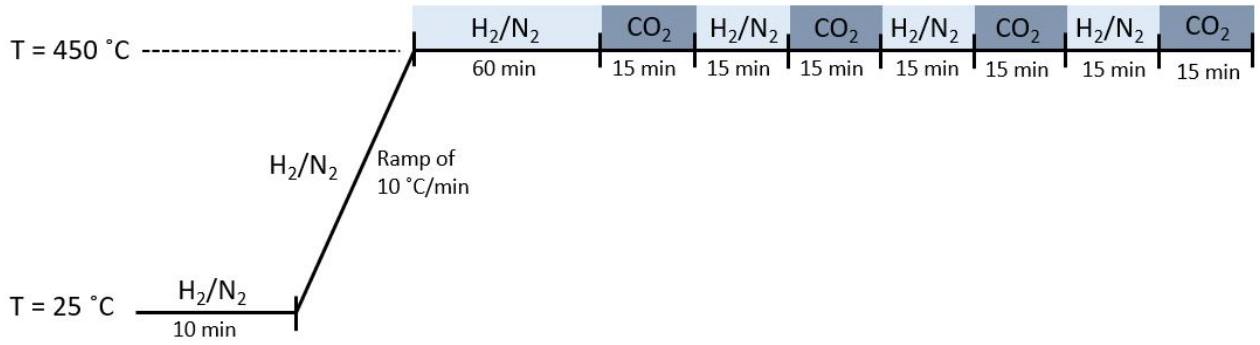

Figure 3.6: A schematic visualization of the proposed protocol for the catalyst screening.

3.5. Hydrogen Quantification Protocol

To determine how much H_2 needs to be supplied in the process, the consumption of H_2 during the reaction needs to be known. To establish the H_2 consumption, a H_2 quantification methodology is developed. For this quantification the MS attached to the reactor setup is utilized. The fixed bed reactor is prepared as described in Section 3.3.1.

To quantify the consumption of H_2, a blank measurement is taken consisting of three cycles. During the blank measurement and the experiment four gasses are used; CO_2, H_2, N_2 and He. A gas flow of 15 mL min^{-1} is utilized for CO_2 and H_2, both for a duration of 150 seconds. Between the CO_2 and H_2 flows, a flow of He (30 mL min^{-1}) is present with a duration of 175 seconds. To ensure a proper functioning of the MS, the H_2 is diluted with 30 mL min^{-1} N_2.

During the blank measurement, the previously specified flow rates are used at room temperature. During the measurements, the gasses are analyzed by IR alpha and MS, where the gasses are visualized as a current. The MS shows the presence of gasses as a current. To convert the current into an amount, a calibration is performed. The current is calibrated using different flow rates of H_2, each consisting of three pulses of 150 seconds. A flow of He is used between the pulses to separate the signals. The H_2 flow rates used for the calibration are 5, 10, 15 and 20 mL/min, all diluted with N_2 till a total flow rate of 45 mL min^{-1}. The area under the curve obtained from the MS, corresponds to a known amount of H_2. Based on these values, a calibration curve is obtained to convert the current into an amount of H_2.

After the blank measurement and its calibration, the temperature is increased to 450 °C under a He and O_2 flow. After the temperature has reached the reaction temperature, a reduction in H_2 takes place. To be able to quantify the H_2 at the higher temperature, another calibration takes place. The procedure for calibrating the experiment is exactly the same as the calibration of the blank measurement. After the calibration has taken place the experiment is performed, consisting of 6 cycles using the previously discussed flow rates. The calibration curve is used to convert the obtained current into an amount of H_2. Figure 3.7 shows a schematic visualization of the protocol to determine the H_2 consumption.

Figure 3.7: A schematic visualization of the protocol to determine the consumption of H_2.

To determine the consumption of H_2 during the experiment, the difference is taken between the amount of H_2 during the blank measurement and during the experiment (Equation 3.4). This difference corresponds to the H_2 consumed during the reaction.

$$H_2 \text{ consumption [mL]} = \int_{t_{H_2,in}}^{t_{H_2,out}} F_{H_2,experiment}(t)dt - \int_{t_{H_2,in}}^{t_{H_2,out}} F_{H_2,blank}(t)dt \tag{3.4}$$

3.6. Methodology of the Economical Analysis

The economic viability of the CCR process is important to determine whether it should be implemented in the current industry. The economic viability is determined by calculating the capital and operating costs and the profitability of the process. The methodology of the *Product and Process Design Principles* written by Seider, Seader, Lewin and Widagdo is used for the economical analysis [28].

3.6.1. Methodology of the Capital Cost Calculation

The capital costs are the one-time expenses to bring a project to an operable status. This includes the purchase of land and equipment, materials used for installation as well as cost of contingencies, and the cost of site preparation.

Multiple methods can be used to calculate the total capital investment, the accuracy is dependent on the method. Seider et al. describes four methods to estimate the total capital investment of the project, each with an increasing level of accuracy [28]. The first method creates an *order-of-magnitude estimate*, based on bench-scale laboratory data to determine the type of equipment. The second method is used for an *study estimate* based on a preliminary process design. When a more detailed process design is known a *preliminary estimate* is made. If the detailed drawings and cost estimates are known the *definitive estimate* can be made, which has the highest level of accuracy. In this thesis the *study estimate* is utilized with an accuracy of ±20%. This preliminary estimate is based on the individual factors method of Guthrie [28]. In the remainder of this section the equations utilized in the estimation are discussed.

The costs to bring a project to an operable status are also known as the total capital investment (C_{TCI}). This value is calculated by adding up the total permanent investment (C_{TPI}) and the working capital (C_{WC}). The working capital is the capital that a business uses in its day-to-day operations, and is estimated as 17.6% of the total permanent investment. The total permanent investment consists of the total bare-module cost (C_{TBM}), the cost of land (C_{site}), the cost of buildings ($C_{buildings}$), and cost of offsite facilities ($C_{offsite}$). Equation 3.5 shows the equation for the total capital investment and Figure 3.8 shows a schematic overview.

$$C_{TCI} = C_{TPI} + C_{WC} = 1.18(C_{TBM} + C_{site} + C_{buildings} + C_{offsite}) + C_{WC} \tag{3.5}$$

The 1.18 visible in equation 3.5 covers a contingency of 15% and a contractor's fee of 3%. In this methodology the royalties and the startup of the plant are not taken into account. The total bare-module cost represents the monetary impact of the process equipment. The total bare-module cost is calculated by taking the sum of the bare-module cost of the equipment pieces present in the process. The cost of site development is estimated as 4-6% of the total bare-module cost, in this analysis a value of 5% is taken [28]. The CCR process will be an addition to an existing process. This means that the cost of buildings is estimated as 5% of the total bare-module cost [28]. The offsite facilities include pollution control, and receiving and shipping facilities. These facilities are estimated as 5% of the total bare-module cost [28].

The previously mentioned bare-module cost of an equipment piece is calculated using:

$$C_{BM} = C_P \frac{I}{I_b}[F_{BM} + (F_d F_p F_m - 1)] \tag{3.6}$$

where:

C_{BM} = bare-module cost;

C_P = purchase cost of equipment;

I = cost index year of analysis (CE = 596) [29];

I_b = cost index of the known cost data (CE = 500);

F_{BM} = bare-module factor of Guthrie;

F_d = equipment design factor;

F_p = pressure factor;

F_m = material factor.

In the CCR process fired heaters and reactors are present. The purchase cost of the equipment is calculated using the equations as mentioned in the *Product and Process Design Principles* book [28]. These will be discussed in the following sections. To utilize these equations the characteristics of the equipment should be known, such as the utility or size.

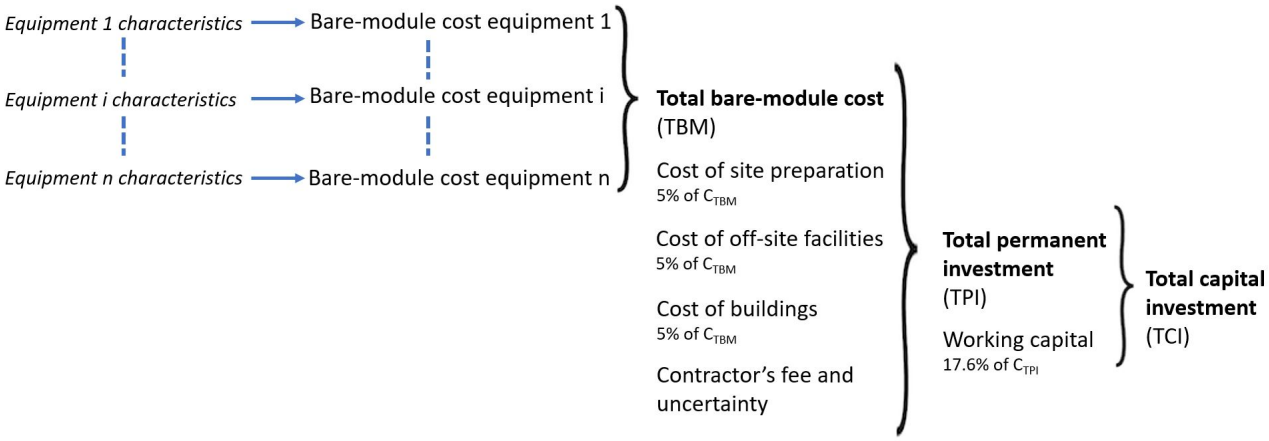

Figure 3.8: Schematic overview for the calculation of the total capital investment for the CCR process.

Cost of Fired Heaters

The purchase cost of the fired heater used in equation 3.6 is determined by:

$$C_P = F_P F_M C_B \tag{3.7}$$

where F_M is the material factor of 1.4 for a fired heater. The pressure factor (F_P) is estimated as 1 when the process occurs at atmospheric pressure. The base cost (C_B) of a fired heater depends on the heat duty (Q) absorbed by the process in Btu/hr. For a cost index of 500 the base cost is determined with:

$$C_B = exp(0.32325 + 0.766[ln(Q)]) \tag{3.8}$$

The calculated purchase cost (C_P) of the fired heater is used in equation 3.6 to calculate the bare-module cost. The bare-module factor (F_{BM}) of Guthrie for a fired heater is 2.19 for ordinary materials of construction, and low-to-moderate pressures [28, 30].

Cost of Reactors

The purchase cost of a reactor is given by:

$$C_P = F_M C_V + C_{PL} \tag{3.9}$$

where F_M is the material factor, C_V represents the cost of the empty reactor, and C_{PL} represents the added cost for platforms and ladders.

The cost of the empty vertical reactor can be estimated using:

$$C_v = exp(7.0132 + 0.18255[ln(W)] + 0.02297[ln(W)]^2) \tag{3.10}$$

where W represents the weight of the reactor in pounds. The weight depends on the wall thickness required for providing rigidity to the reactor. At low pressures a minimum wall thickness (t_s) is used as an approximation. The weight of the reactor is calculated by:

$$W = \pi(D + t_s)(L + 0.8D)t_s\rho \tag{3.11}$$

where L corresponds to the height of the reactor in feet, D the inside diameter of the reactor in feet, t_s the previously mentioned wall thickness and ρ the density of carbon steel.

The cost for platforms and ladders for vertical reactor is calculated using:

$$C_{PL} = 361.8(D)^{0.73960}(L)^{0.70684} \tag{3.12}$$

where D is the inside diameter in feet, and L the length of the reactor.

By using equation 3.6 and the calculated values for platforms and ladders (C_{PL}), and the cost for the empty vertical reactor (C_V) the bare-module cost is calculated. The bare-module factor (F_{BM}) of Guthrie for a reactor is 4.16 for ordinary materials of construction and low-to-moderate pressures [28, 30].

3.6.2. Methodology of Operating Cost Calculation

The operating cost are the expenses that are related to the operation of a business. These cost are separated into two groups: the feedstock costs, and ancillary costs. The ancillary costs includes the utilities, maintenance, fixed costs, and the general expenses. In this analysis the labor-related costs are not taken into account.

The cost of feedstock is determined by multiplying the inflow of the feedstock with the buying price of that feedstock. The utilities needed during the production can have a significant impact on the cost of the process. For this analysis, it is assumed the utilities are purchased from a different company, however it is a possibility for a company to build its own utility plant. In the CCR process the cost for utilities are due to heating the feedstocks. The cost is calculated by multiplying the consumption of the utility with its buying price.

During the operation, regular maintenance should occur to ensure a safe and proper operating process. The cost of maintenance is related to the materials and services required for a working process. The materials and service for maintenance are assumed to be 5% of the total permanent investment [28]. Another part of the annual cost of maintenance is the maintenance overhead which can be estimated as 0.25% of the total permanent investment [28]. So the yearly maintenance of the CCR process is estimated as 5.25% of the total permanent investment of the process.

Other costs that are not dependent on the plant operations are the property taxes and insurances, rental fees, depreciation and licensing fees. The rental and licensing fees are not present in the process, so are not taken into account in the analysis.

The annual property taxes are determined by the local municipality as a percentage of the total permanent investment. This can range between 1% for a process in a sparsely populated area to 3% for a process in a heavily populated areas [28]. For this analysis a heavily populated area is taken, so the annual property tax will be taken as 3% of the total permanent investment.

The annual insurance for the process is dependent on the level of risk and can be approximated as a percentage of the total permanent investment. Considering a CCR process operated at relatively mild temperatures and ambient pressure, 0.5% of the total permanent investment is used [28].

The depreciation of materials is the last fixed cost element taken into account in this analysis. The depreciation measures the decrease in value of an asset throughout time. A multitude of methods can be used to approximate the depreciation. A rough estimation is made by using a straight-line depreciation. This means that the process has no worth at the end of its lifetime and that the depreciation is taken as a constant percentage of the total permanent investment. In this analysis a lifetime of 15 years is taken. The yearly depreciation can therefore be estimated as 6.7% of total permanent investment.

Total Production Cost

To determine the total cost of manufacture the cost for feedstock, utilities, maintenance and the fixed costs are summed up. The general expenses are added to these cost to calculate total annual operating costs. The general expenses refer to activities that occur centrally in a company and are financed from the profits made by the company. These general expenses are assumed to be a percentage of the sales, in this analysis a percentage of 9.55 is taken [28].

3.6.3. Profitability Analysis

The annual gross earnings is the difference between the annual sales revenue and the previously determined annual operating cost. The annual sales revenue are calculated by multiplying the yearly syngas production with the selling price of the product. To calculate the yearly net earnings the tax rate should be taken into account. The tax rate depends on the country and the legal form of the company, in this analysis a tax rate of 25% is used. The net earning is approximated by:

$$\text{Net earnings} = (1 - t)(S - C) \tag{3.13}$$

where t is the income tax rate, S the annual sales revenue, and C the annual operating cost.

For an investment to be worthwhile for a company a large annual net earning is not sufficient. The profit over the lifetime of the process should be greater than the original capital investment of that process. To analyze the profitability of a process a number of measures have been developed. These can be used by companies to analyze which alternative venture is more suitable. A profitability measure that is widely used in early evaluations is the payback period due to its simplicity. The payback period (PBP) is the time required for the annual earnings to be equal to the original investment. Several definitions exist to calculate the payback period, in this analysis the definition of Seider et al. is used [28].

$$\text{PBP} = \frac{\text{total permanent investment}}{\text{net earnings} + \text{annual depreciation}} = \frac{C_{TPI}}{(1 - t)(S - C) + D_{process}} \tag{3.14}$$

It should be noted that the PBP is an approximate measure that does not take the time value of money into account. As a consequence, when the project evaluation is more advanced the payback period should be re-evaluated before a final decision is made whether to proceed with this process.

4

Characterization Results

In this chapter the results of the different characterization methods are discussed. Section 4.1 describes the results of the XRD and Section 4.2 the results of the SEM. The results obtained from the N_2 adsorption measurements are discussed in Section 4.3.

4.1. XRD Results

In Figure 4.1 the diffractograms are given for fresh Cu-K/γ-Al_2O_3 type 1 and type 2. No clear difference between these two catalyst is found in while using XRD, only the intensity of some reflexes differ between the two samples. Type 1 has a slightly longer measurement time (1 hour) which results in reduced noise in the diffractogram. In the diffractograms the compounds CuO tenorite and γ-Al_2O_3 are clearly visible. The γ-Al_2O_3 has defined reflexes at 46° and 66°. Most of the other reflexes are attributed to CuO tenorite, of which the main reflexes are visible at 35° and 39°. The reflexes that are not indicated by the CuO or γ-Al_2O_3 can be attributed to potassium dawsonite ($KAl(CO_3)(OH)_2$) [31]. No K_2CO_3 reflexes are detected in the diffractogram. This indicates that a highly dispersed K phase is present on the catalyst surface at room temperature.

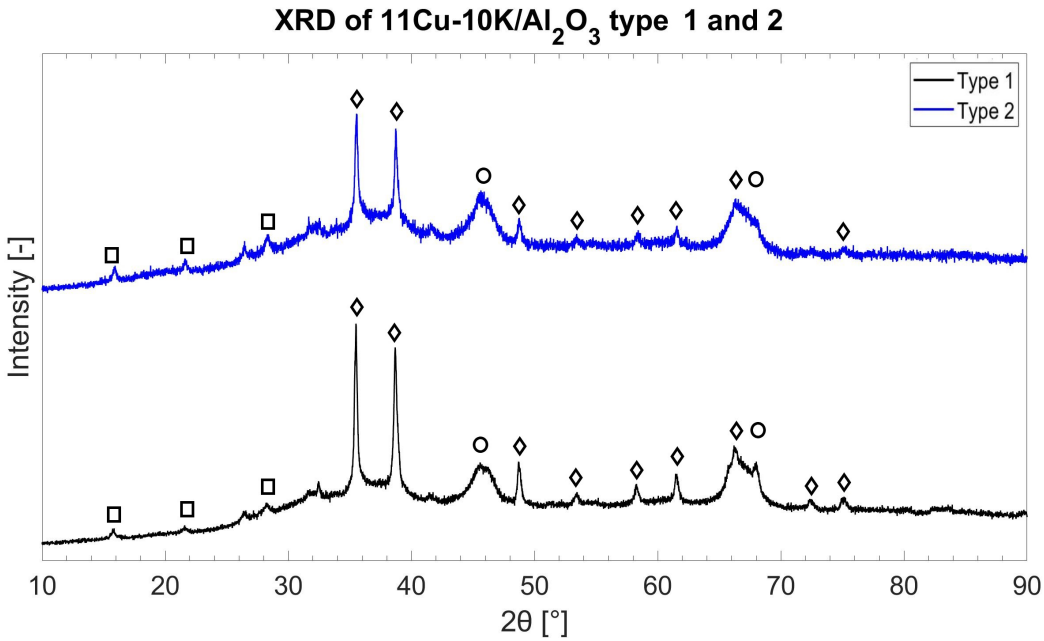

Figure 4.1: X-ray diffractograms of fresh 11Cu-10K/γ-Al_2O_3 type 1 and 2 obtained at room temperature. Phase identification: γ-Al_2O_3 (○), potassium dawsonite (□) and CuO (⋄).

In Figure 4.2 the diffractogram is given for the fresh FeCrCuK/PMG20 catalyst. Most reflexes are attributed to the PMG20 support. The reflexes at 37°, 45° and 65° are caused by spinel $MgAl_2O_4$ and γ-Al_2O_3. The γ-Al_2O_3 also causes a reflex at 21°. The reflex at 32° can be attributed to K_2CO_3 and the reflex at 36° to Fe_2O_3 hematite. The diffraction reflexes associated to Cu and Cr phases were not observed. This is likely due to a high dispersion and low concentrations [12].

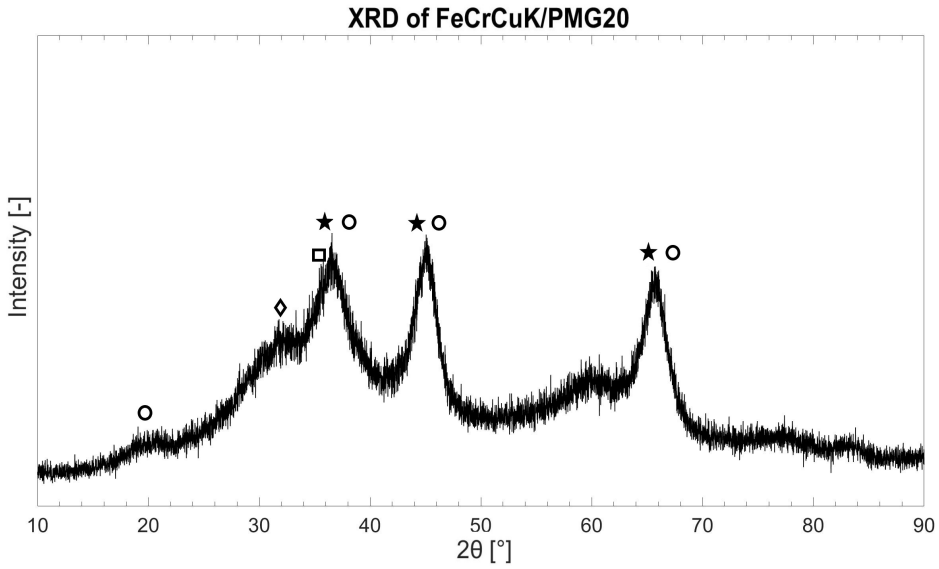

Figure 4.2: X-ray diffractogram of fresh FeCrCuK/PMG20 obtained at room temperature. Phase identification: γ-Al_2O_3 (○), $MgAl_2O_4$ (⋆), K_2CO_3 (⋄) and Fe_2O_3 (□).

4.2. SEM and EDS Results

This section discusses the images obtained from SEM and EDS. The measurements were performed on fresh Cu-K/γ-Al_2O_3 type 1 and 2, and fresh FeCrCuK/PMG20 catalyst.

Cu-K/γ-Al_2O_3

Figure 4.3 shows the SEM results for Cu-K/γ-Al_2O_3 type 1 and 2. In Figures 4.3a and 4.3c the secondary electron imagining (SEI) is visualized with a magnification of 350. When using a greater magnification (Figures 4.3b and 4.3d) 'needle-like' crystal structures are observed. These aggregates are seen on the γ-alumina surface as well as on K_2CO_3-promoted hydrotalcites, and are assigned to hydrates of potassium carbonate [32]. The diffractogram in Figure 4.1 suggests that those species can be related to the crystalline phase of potassium dawsonite. No clear morphological differences are visualized between type 1 and type 2 using SEM.

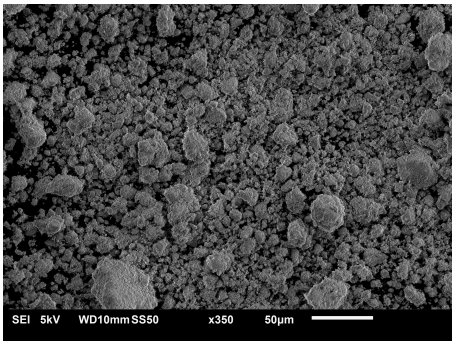

(a) Secondary electron imagining (SEI) of catalyst surface of Cu-K/Al_2O_3 type 1 (x350 magnification).

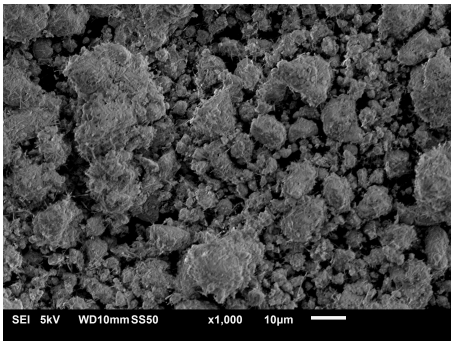

(b) Secondary electron imagining (SEI) of catalyst surface of Cu-K/Al_2O_3 type 1 (x1000 magnification).

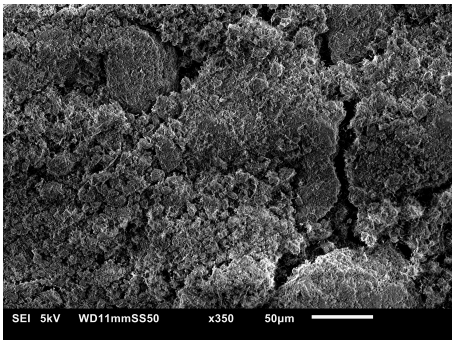

(c) Secondary electron imagining (SEI) of catalyst surface of Cu-K/Al_2O_3 type 2 (x350 magnification).

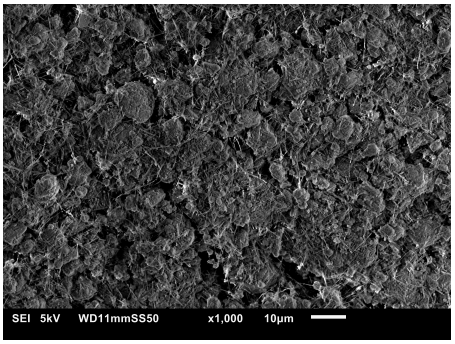

(d) Secondary electron imagining (SEI) of catalyst surface of Cu-K/Al_2O_3 type 2 (x1000 magnification).

Figure 4.3: SEM images of fresh 11Cu-10K/γ-Al_2O_3 type 1 (a, b) and 2 (c,d) at different magnifications.

To analyze the dispersion of Cu and K, back-scattered electron imaging is used. From back-scattered electron imagining it is seen that some agglomerated Cu crystallites are present, however a majority is highly dispersed over the surface. The degree of dispersion for both Cu and K can further be confirmed by the energy-dispersive spectroscopy (EDS) seen in Figure 4.4. In the EDS, the aforementioned agglomeration is also visualized, since the density is higher at certain spots. It has to be remarked that the measurement only occurs at a certain location on the catalyst particle, so the degree of dispersion or agglomeration can fluctuate across the fresh catalyst. Furthermore, the 'needle-like' crystal structures are not visible on the elemental maps due to the size of these structures. Due to this, the visualization of the elements can deviate from the real bulk composition. From the EDS it is determined that there are no contaminants detected in the sample. Furthermore, the EDS can be used to determine the composition based on the relative masses of Al, Cu and K. Based on the relative masses, the ratio between Cu and K is roughly one for both catalyst types. This means that for both types of Cu-K/γ-Al_2O_3 the aimed ratio is obtained.

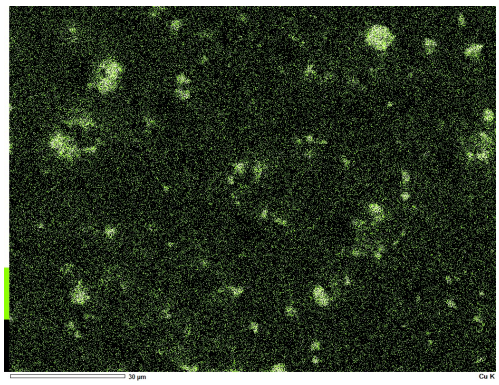

(a) Elemental map of Cu.

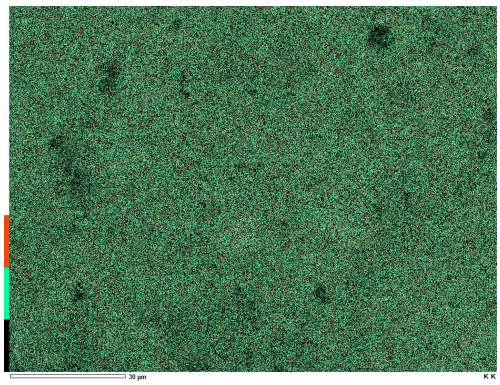

(b) Elemental map of K.

Figure 4.4: Elemental maps obtained by EDS using the back-scattered electron composition of fresh Cu-K/γ-Al_2O_3 type 1 (x1000 magnification).

FeCrCuK/PMG20

Figure 4.5 shows the secondary electron imagining of the catalyst surface of FeCrCuK/PMG20. The previously mentioned 'needle-like' are also observed when using greater magnification. The aggregates are assigned to hydrates of potassium carbonate [32].

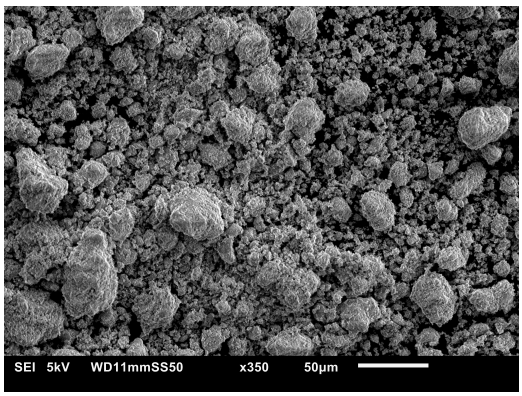

(a) Secondary electron imagining (SEI) of catalyst surface of FeCrCuK/PMG20 (x350 magnification).

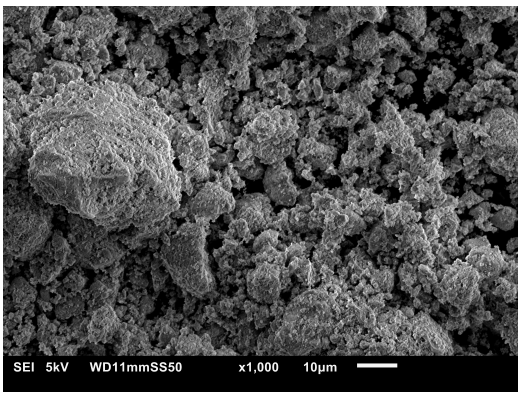

(b) Secondary electron imagining (SEI) of catalyst surface of FeCrCuK/PMG20 (x1000 magnification).

Figure 4.5: SEM images of fresh FeCrCuK/PMG20 catalyst at different magnifications.

To analyze the dispersion of Fe and K, back-scattered electron imaging is used. The dispersion of these two metals is determined due to their presence in the catalyst compared to the other metals. The degree of dispersion is visualized in Figure 4.6. Both Fe (Figure 4.6a) and K (Figure 4.6b) are highly dispersed. The degree of dispersion and agglomeration can fluctuate across the catalyst surface as discussed previously. No contaminants are detected in the sample.

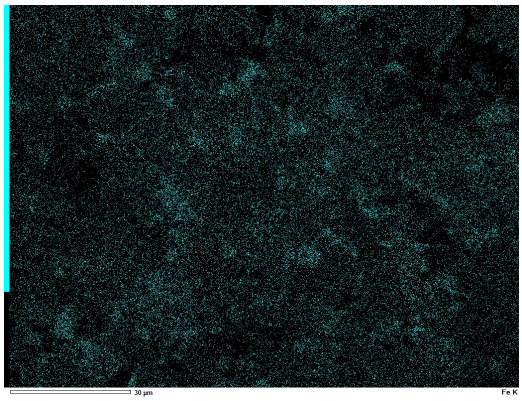

(a) Elemental map of Fe of the FeCrCuK/PMG20 catalyst.

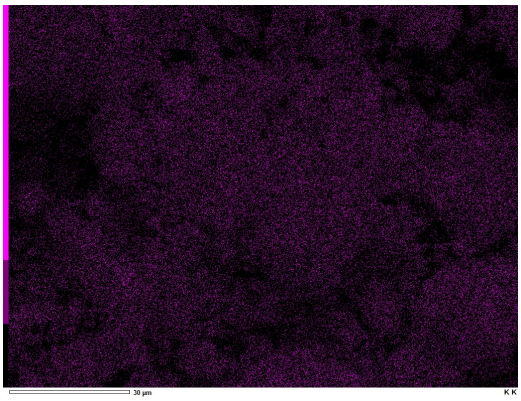

(b) Elemental map of K of the FeCrCuK/PMG20 catalyst.

Figure 4.6: Elemental maps obtained by EDS using the back-scattered electron composition of fresh FeCrCuK/PMG20 catalyst.

4.3. Surface Area and Pore Volume Results

This section discusses the results of the surface area and pore volume obtained from the N_2 adsorption experiment. The isotherm linear plots are found in Appendix A.

Using the method discussed in Section 3.2.3, different samples have been characterized. The samples that have been characterized are the fresh Cu-K/γ-Al_2O_3 type 1 and 2, fresh FeCrCuK/PMG20, and the PMG20 support itself. Furthermore, to determine the amount of Milli-Q needed for the K impregnation for Cu-K/γ-Al_2O_3, the pore volume of Cu/γ-Al_2O_3 is determined. The surface area and pore volume of these samples is specified in Table 4.1.

Table 4.1: The BET surface area and the pore volume of the samples.

Material	**BET surface area** [$m^2\,g^{-1}$]	**Pore volume** [$cm^3\,g^{-1}$]
γ-Al_2O_3	255	0.8 - 1.2
Cu/γ-Al_2O_3	196	0.62
Cu-K/γ-Al_2O_3 Type 1	120	0.42
Cu-K/γ-Al_2O_3 Type 2	148	0.48
PMG20	233	0.55
FeCrCuK/PMG20	75	0.21

Table 4.1 shows the promotion of the catalyst support decreases the surface area and pore volume significantly. The impregnation of the metal is linked to pore blocking of the porous support, which results into the drop of the available BET surface area. After all the metals are impregnated the lowest BET surface area is obtained. Interestingly, Cu-K/γ-Al_2O_3 type 1 and 2, which have the same aimed catalyst composition, show different porosity and surface area values. This indicates that the modification of the synthesis method has an impact on the final properties of the catalyst.

5 Results of the Experiments

This chapter discusses the results of the experiments performed using the methodology described in Chapter 3. The results obtained from catalyst screening is found in Section 5.1. Section 5.2 highlights the CO_2 capacity and CO production from the different catalysts. The H_2 quantification is discussed in Section 5.3.

5.1. Catalyst Screening Results

To determine the CO_2 capacity of the samples TGA is employed using the protocol described in Section 3.4. To determine the CO_2 capture capacity of the samples, the weight increase experienced in CO_2 atmosphere is recorded and evaluated for two different sets of experiments, involving CO_2/H_2 pulses or CO_2/N_2 pulses.

In Figure 5.1 the weight change over time is visualized while switching between H_2 and CO_2 for different sample compositions. The weight change is normalized with the catalyst weight obtained after the initial reduction pre-treatment. In the figure only the weight change occurring due to alternating CO_2 and H_2 is visualized, the thermogravimetric profile of the complete experiment can be found in Appendix B.1.

Three samples are tested: K/γ-Al_2O_3, Cu/γ-Al_2O_3, and Cu-K/γ-Al_2O_3 type 1. It is known that alkaline metals, such as K, introduce the CO_2 capture functionality in the catalytic material. An unpromoted Cu/γ-Al_2O_3 catalyst is tested as reference in the CO_2/H_2 experiment to ensure that the observed catalyst weight increase in CO_2 is attributed to its sorption on K. As can be seen in Figure 5.1, no significant weight increase occurs in the unpromoted Cu/γ-Al_2O_3 sample. Furthermore, a weight increase does take place when solely K is present. If both metals are present, a higher weight increase is observed. The weight loss in H_2 observed for K/γ-Al_2O_3 and Cu-K/γ-Al_2O_3 type 1 seems to follow a different rate. This confirms that the presence of Cu in the catalyst has an influence on the occurring CO_2 capture and reduction, enhancing the removal of the captured CO_2 species.

Experiments performed in the reactor setup showed that when only K is present as a metal, no capture occurs during the second cycle [33]. From 5.1 it is seen that a weight change does take place in the second cycle when using the TGA. This indicates that, in the TGA setup configuration, additional phenomena besides CO_2 capture may contribute to the weight increase. The weight increase that occurs for Cu-K/γ-Al_2O_3 type 1 when switching between H_2 and CO_2 is 14.4 mg/g_{cat} considering the average of the last three cycles. Based on the discrepancies observed between the TGA results and the catalytic tests in the reactor setup, this weight increase cannot be directly assigned to the amount of CO_2 captured by the catalyst. To distinguish the CO_2 capture from the additional occurring phenomena, an additional experiment is performed.

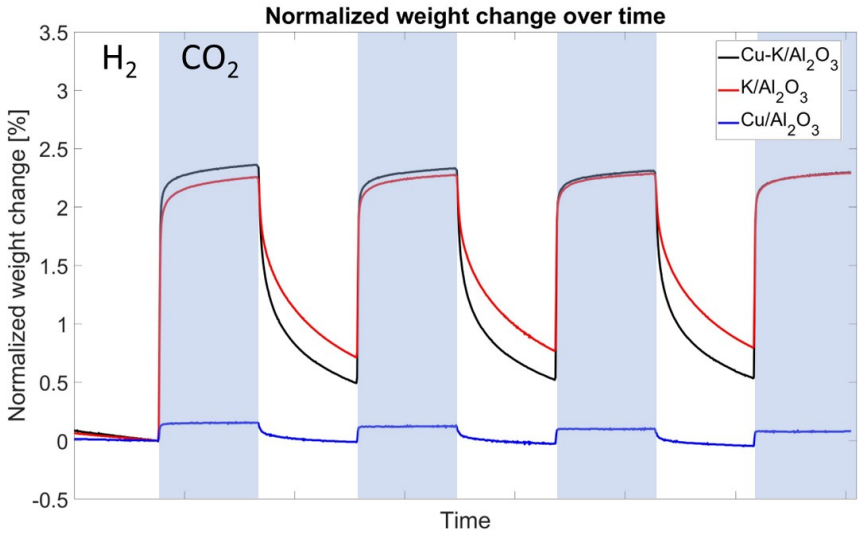

Figure 5.1: TGA of Cu/γ-Al_2O_3, K/γ-Al_2O_3, and Cu-K/γ-Al_2O_3 type 1 performed by alternating CO_2 and H_2.

This additional experiment is performed by substituting H_2 with N_2. H_2 is fundamental to regenerate the CO_2 capture active sites in Cu-K/γ-Al_2O_3. By substituting H_2, a loss of continuous activity of capture and reduction is expected. Two samples are tested: K/γ-Al_2O_3 and Cu-K/γ-Al_2O_3 type 1.

Figure 5.2 visualizes the weight change over time while switching between N_2 and CO_2. Interestingly, a weight increase is still visible in the presence of CO_2. The weight change observed for both samples seems to follow the same rate. This clearly shows that the occurring phenomenon is developed by the presence of K in the system, independently from the presence of Cu.

The weight increase for Cu-K/γ-Al_2O_3 type 1 is 11.8 mg/g_{cat} considering the last three cycles.

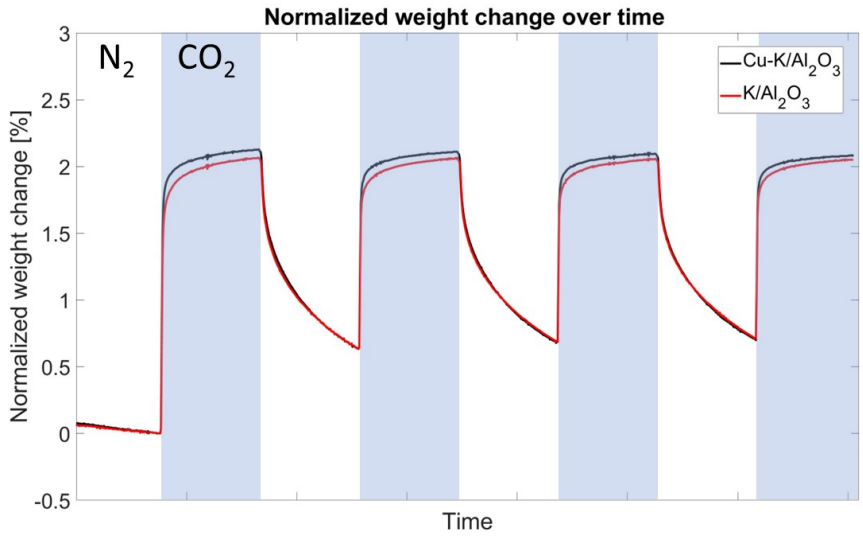

Figure 5.2: TGA of K/γ-Al_2O_3 and Cu-K/γ-Al_2O_3 type 1 performed by alternating CO_2 and N_2.

The hypothesis is that the difference between the weight increase between the CO_2/N_2 and CO_2/H_2 experiment represents the CO_2 capture observed in CCR conditions. To confirm that, a similar experiment is performed in the reactor setup, with the addition of a He-flush between the switching of the reactants. The flowrate of the gasses is 50 mL min^{-1} and the experiment is performed at 450 °C after an hour long reduction in H_2 or passing N_2 to the reactor.

In Figure 5.3 the result obtained from switching between CO_2 and H_2 in the reactor setup is visualized. It is seen that CO_2 capture occurs, as well as a reduction into CO. A quick reduction occurs due to high flows used in this experiment. In contrast, Figure 5.4 shows the catalytic behaviour when switching between CO_2 and N_2. It can be seen that no CO_2 capture occurs, and subsequently no CO production. This confirms the importance of H_2 in generating the active phase for capture by selectively removing the captured CO_2 in the form of CO.

From the experiment visualized in Figure 5.3 the capture of CO_2 can be determined. This results in a capture of 62 µmol/g_{cat}. Regarding the TGA results, the CO_2/N_2 experiment can be considered as a blank measurement. This measurement accounts for additional phenomena responsible for the weight increase not strictly related to the catalytic CO_2 capture and reduction. In fact, by subtracting the weight increase observed during the CO_2/N_2 experiment, from the weight increase occurring during the switching between H_2/CO_2, a weight uptake of 2.6 mg/g_{cat} is obtained. This corresponds to 60 µmol/g_{cat}, which is clearly in agreement with the results obtained from the catalytic test in the reactor setup.

However, there is no knowledge on the relevant weight increase observed in the CO_2/N_2 experiment in the TGA. Further research is required to understand the exact phenomena causing this increase. It is possible that the cause is an interaction of the gas with the catalyst in the TGA which is not visible in the reactor setup. During catalytic tests, the gas flows through the catalyst bed, while in the TGA the gas flows over the crucible. Based on the results and the uncertainty surrounding the occurring weight increase, the CO_2 capacity in the remainder of this thesis is determined using the reactor setup.

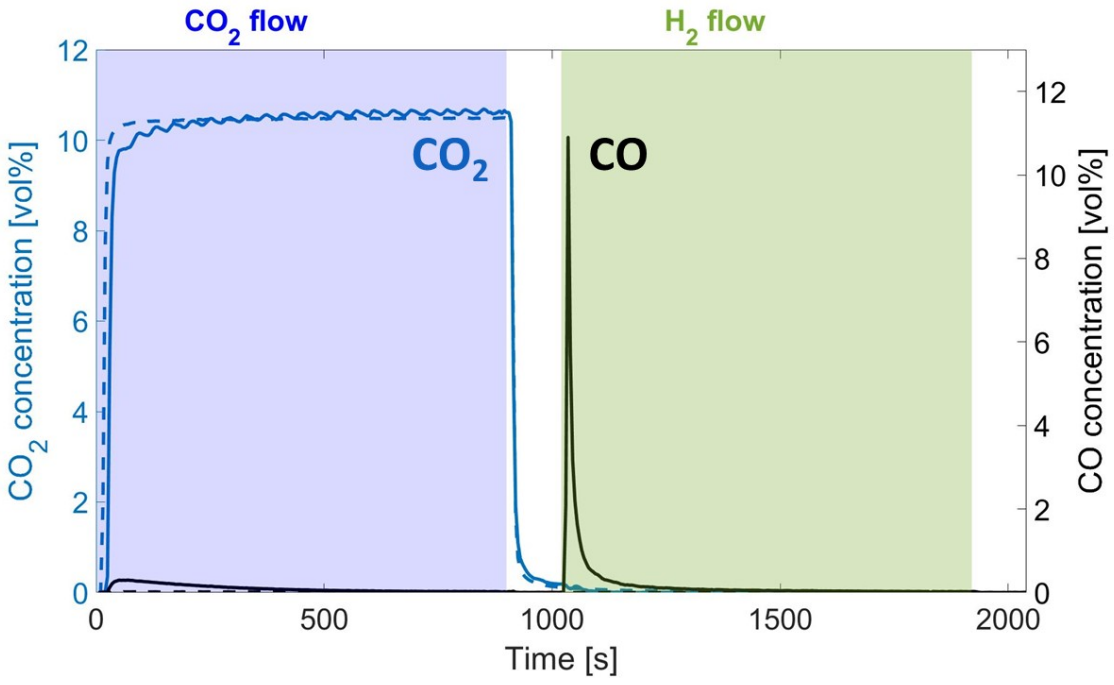

Figure 5.3: Catalytic behaviour of 200 mg Cu-K/γ-Al_2O_3 type 1 at 450 °C when switching between H_2 and CO_2.

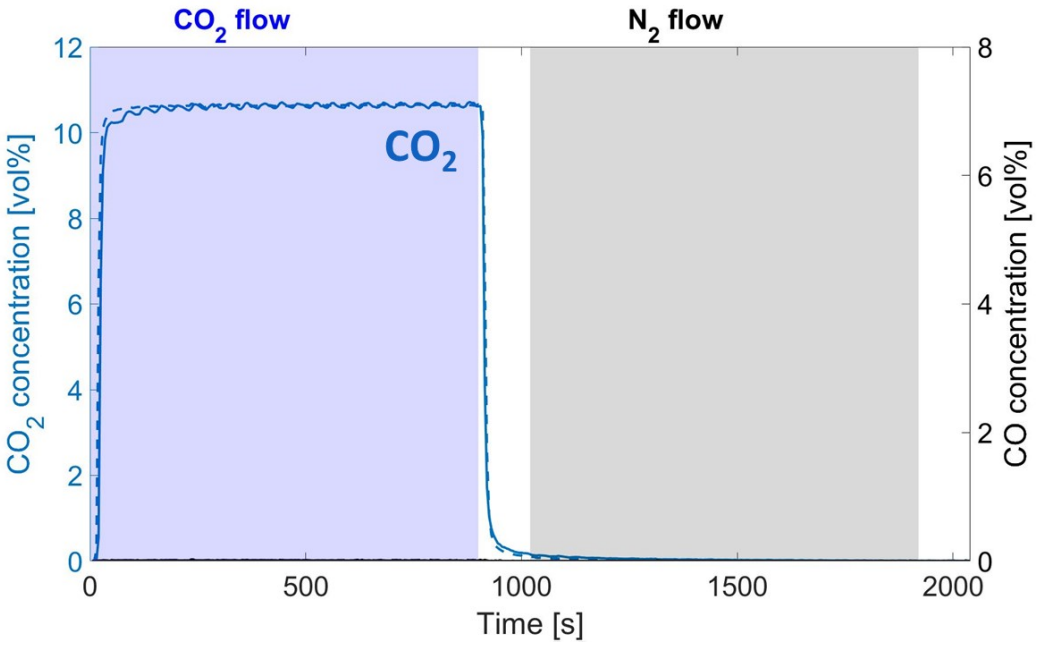

Figure 5.4: Catalytic behaviour of 200 mg Cu-K/γ-Al_2O_3 type 1 at 450 °C when switching between N_2 and CO_2.

5.2. Reactor Setup Results

This section discusses the results obtained from the reactor setup. First of all, the results from testing Cu-K/γ-Al_2O_3 are described and visualized. Secondly, results obtained from the FeCrCuK/PMG20 are discussed.

Figures 5.5 and 5.6 show the results of the catalytic test of Cu-K/γ-Al_2O_3 type 1 and 2. The experiment consists of a capture and reduction phase of 420 seconds, separated by a He-flush phase of 175 seconds. The dashed line is the concentration obtained from the blank measurement, performed on fresh catalyst at room temperature. As expected, no production of CO is visible during the blank measurement. The delay between the automatic valve switching and the collection of the stream at the outlet is responsible for the offset of the concentration signals with respect to the feed pulses. By using the blank measurement, the interaction of gas mixtures with the catalyst and possible mass flow and diffusion limitations are taken into account. The CO_2 capture occurring in the capture phase is the difference between the dashed and continuous line as mentioned in Section 3.3. Figures 5.7 and B.3 show the release of H_2O during the capture of CO_2. The generation of H_2O in the capture phase indicates the presence of active H or OH species [34]. Research suggests that during the capture phase carbonates species are formed (reaction R5.1) [34].

$$2\,\mathrm{KOH} + \mathrm{CO_2} \leftrightarrow \mathrm{K_2CO_3} + \mathrm{H_2O} \tag{R5.1}$$

In Figures 5.5 and 5.6 the CO production occurring in the experiment is denoted with a red line. It is seen that during the capture phase limited amounts of CO are produced after full CO_2 capture takes place. The CO production can occur due to weakly retained H_2 on the catalyst surface, which can take part in CO_2 hydrogenation [34, 35, 36]. The presence of low amounts of CO in the CO_2-free exhaust gas is undesired, since it represents a toxic and corrosive gas. However, CO is only detected after the majority of the active sites for CO_2 capture are occupied. Previous works have proved that CO can be efficiently captured by the active catalyst [35]. This means that in an optimized process with full capture of CO_2, this reaction pathway will not play a relevant role.

During the He-flush no significant production of CO or CO_2 is detected. This confirms that the species are strongly adsorbed on the catalyst surface. For both types of catalysts, the CO production occurs mainly in the reduction phase. Most of the CO production occurs during the first 150 seconds as a fast peaked release, followed by a continuous tailing of the CO signal. The fast CO production shows that the formed carbonates during the capture phase are quickly decomposed. This fast release is not coupled with H_2O generation (Figures 5.7 and B.3).

A possible reaction path for the fast release is [34]:

$$K_2CO_3 + H_2 \leftrightarrow 2\,KOH + CO \tag{R5.2}$$

After this fast release of CO, a long tailing of CO formation takes place. During this CO production a H_2O signal is observed. This production can occur due to the slow decomposition of formates to CO and H_2O [34].

An interesting property of Cu-K/γ-Al_2O_3 is the absence of CO_2 release during the reduction phase. This reveals a highly selective conversion of the captured CO_2 to CO. The CO_2 capture capacity of Cu-K/γ-Al_2O_3 type 1 is 226 µmol g^{-1}, determined using Equation 3.1. The CO_2 capacity of the type 2 catalyst is 192 µmol g^{-1}. The CO production rate is 0.50 µmol g^{-1} s^{-1} and 0.43 µmol g^{-1} s^{-1} for Cu-K/γ-Al_2O_3 type 1 and type 2, respectively.

The two catalysts do not show unusual structural (Figure 4.1) or morphological (Figure 4.3) characteristics that could explain the distinct catalytic performance. However, the N_2 adsorption measurement returned a higher surface area and pore volume for catalyst type 2 (Table 4.1). Considering that the reaction occurs at the surface area of the catalyst, the expectation is that type 2 outperforms type 1. The higher pore volume of catalyst type 2 did not result in a higher catalytic activity. The reason can be attributed to a difference in dispersion of Cu and K compared to catalyst type 1. The dispersion and contact between the Cu and K phases is vital to ensure the capture of CO_2 and its selective reduction. Another explanation of the difference in catalytic behaviour can be the higher relative amount of Cu and K present in catalyst type 1. The higher relative amount is a consequence of the presence of significant amounts of water adsorbed in the γ-Al_2O_3 weighed for synthesis. A weight loss of 12.8 wt% can occur when heating the catalyst to remove the adsorbed H_2O [27]. This weight loss can result in a relative higher content of Cu and K in the final catalyst used in the reactor setup. Further investigation needs to be conducted to determine the exact catalyst loading with quantitative techniques such as ICP-MS.

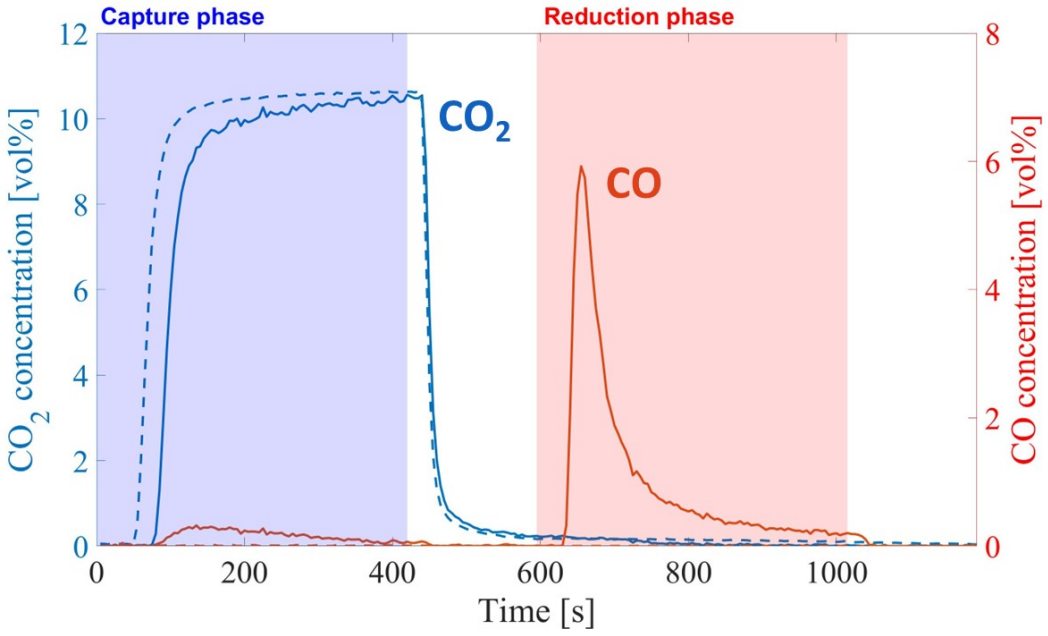

Figure 5.5: Catalytic behaviour of 200 mg Cu-K/γ-Al_2O_3 type 1 at 450 °C. During the experiment flows of CO_2 of 15 mL min^{-1}, H_2 of 15 mL min^{-1} and a He-flush of 30 mL min^{-1} are used. The duration of the capture and reduction phase is 420 seconds, the He-flush phase is 175 seconds.

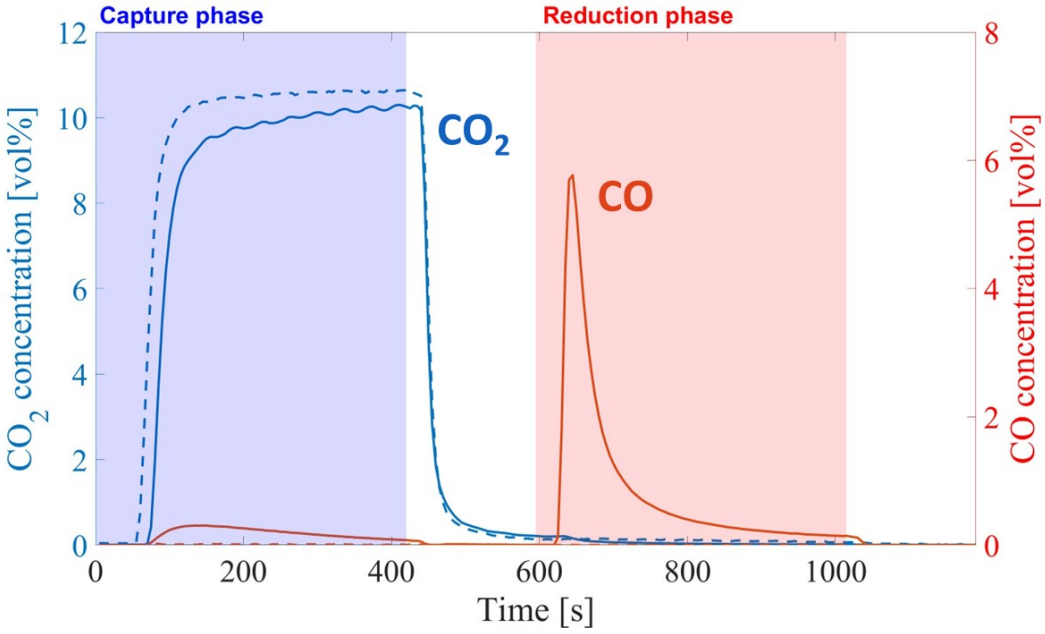

Figure 5.6: Catalytic behaviour of 200 mg Cu-K/γ-Al_2O_3 type 2 at 450 °C. During the experiment flows of CO_2 of 15 mL min^{-1}, H_2 of 15 mL min^{-1} and a He-flush of 30 mL min^{-1} are used. The duration of the capture and reduction phase is 420 seconds, the He-flush phase is 175 seconds.

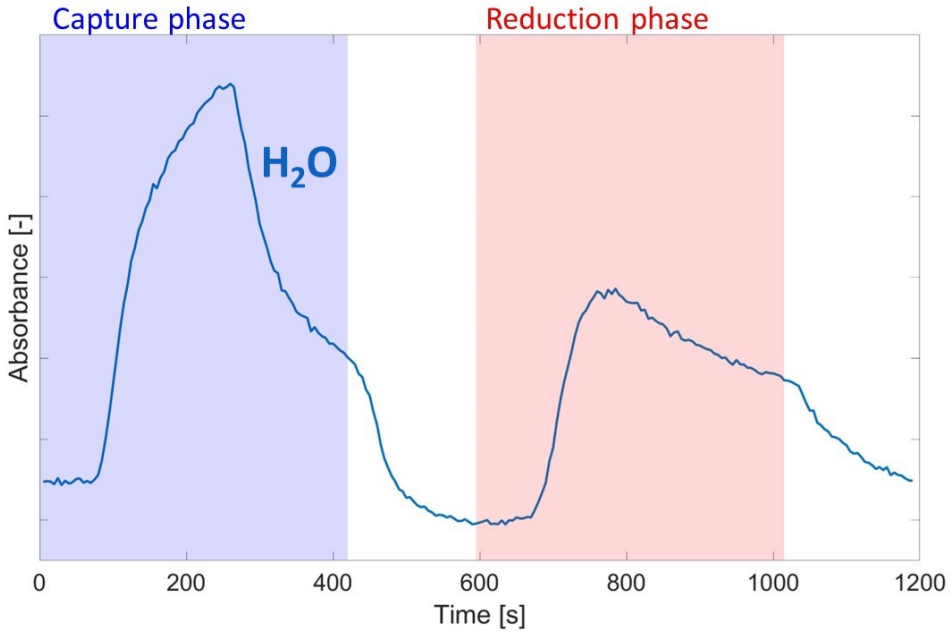

Figure 5.7: H_2O profile of Cu-K/γ-Al_2O_3 type 1 at 450 °C. During the experiment flows of CO_2 of 15 mL min^{-1}, H_2 of 15 mL min^{-1} and a He-flush of 30 mL min^{-1} are used. The duration of the capture and reduction phase is 420 seconds, the He-flush phase is 175 seconds.

From the previously discussed results it is seen that most of the CO production occurs at the beginning of the reduction phase. To reduce the excess amount of H_2 utilized in this process, the duration of the reduction phases can be shortened. The duration of the capture and reduction phases have been set equal in this thesis to meet the requirements of a continuous operation in a two-reactor type of plant. Taking the shorter CO production into account the experiments are performed using a capture and reduction phase duration of 150 seconds. Figures 5.8 and 5.9 show the results obtained from Cu-K/γ-Al_2O_3 type 1 and type 2.

For both catalyst types it is seen that CO_2 capture during the capture phase is clearly visible. At shorter phase durations the production of CO during the capture phase is still visible. During the reduction phase, the peak of CO production is clearly visible, however the tail that could be seen in Figures 5.5 and 5.6 is less pronounced. This also has an impact on the CO_2 capacity of the catalyst. The CO_2 capacity of Cu-K/γ-Al_2O_3 type 1 is 128 µmol g^{-1} with a CO production rate of 0.78 µmol g^{-1} s^{-1}. The CO_2 capacity of Cu-K/γ-Al_2O_3 type 2 is 116 µmol g^{-1} with a CO production rate of 0.72 µmol g^{-1} s^{-1}. During these experiments, H_2O production in the reduction phase occurs less pronounced compared to the longer experiment (Figure B.4). This can be attributed to the reduced CO tail, which is the cause for the H_2O production in the reduction phase.

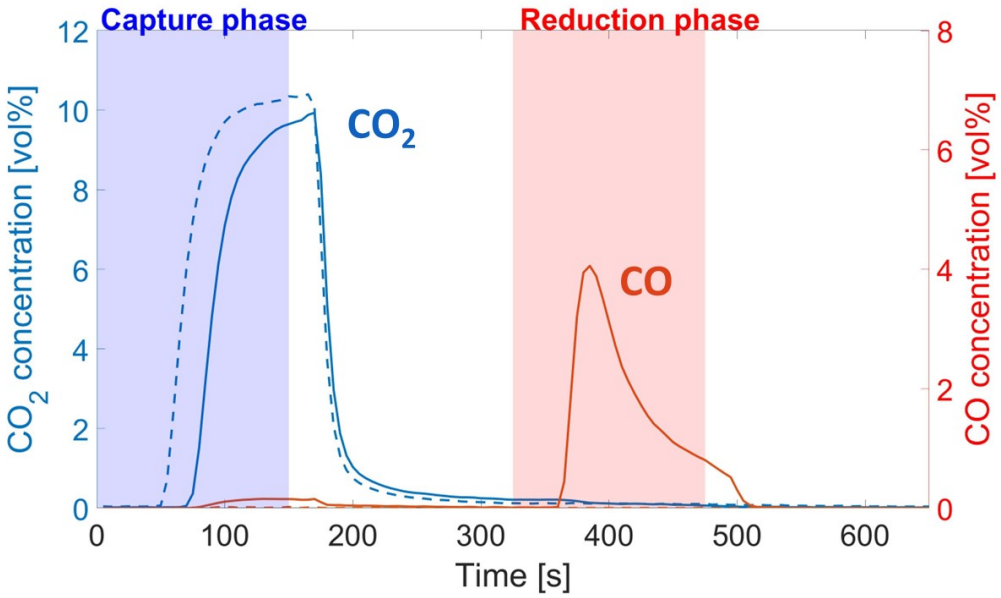

Figure 5.8: Catalytic behaviour of 200 mg Cu-K/γ-Al_2O_3 type 1 at 450 °C. During the experiment flows of CO_2 of 15 mL min^{-1}, H_2 of 15 mL min^{-1} and a He-flush of 30 mL min^{-1} are used. The duration of the capture and reduction phase is 150 seconds, the He-flush phase is 175 seconds.

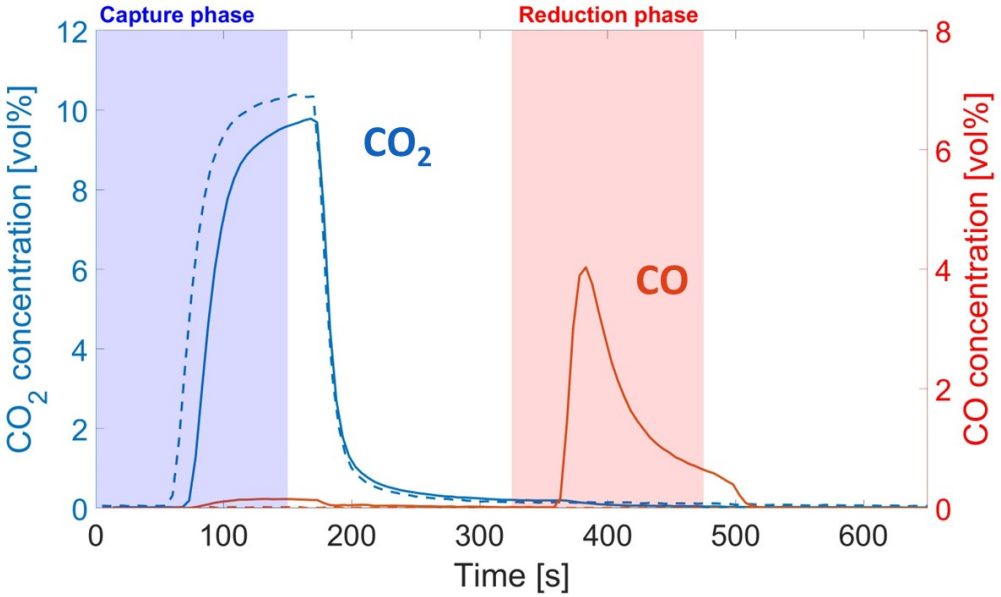

Figure 5.9: Catalytic behaviour of 200 mg Cu-K/γ-Al_2O_3 type 2 at 450 °C. During the experiment flows of CO_2 of 15 mL min^{-1}, H_2 of 15 mL min^{-1} and a He-flush of 30 mL min^{-1} are used. The duration of the capture and reduction phase is 150 seconds, the He-flush phase is 175 seconds.

Besides the previously discussed Cu-K/γ-Al_2O_3 also the catalytic behaviour of FeCrCuK/PMG20 is tested. Figure 5.10 shows the catalytic results of FeCrCuK/PMG20. Clear differences are seen when compared to the catalytic results of Cu-K/γ-Al_2O_3. Significant CO_2 capture occurs during the capture phase. However, a significant CO production also takes place after full capture has been achieved.

From the XRD it could be seen that at ambient conditions Fe_2O_3 hematite is present (see Section 4.1). In the presence of H_2, a part of the Fe_2O_3 reduces to Fe_3O_4 magnetite, with further reduction to FeO or Fe. The production of FeO takes place more often compared to Fe if there is a presence of H_2O. As seen in Figure 5.11, significant H_2O production occurs in the reduction phase. This indicates that production of FeO takes place, which can be followed by the production of Fe_3O_4.

Figure 5.10 shows that, after full CO_2 capture is achieved in the capture phase, significant CO production takes place. Due to the presence of FeO and Fe_3O_4 after reduction, the CO production can occur via:

$$2\,Fe_3O_4 + CO_2 \leftrightarrow 3\,Fe_2O_3 + CO \tag{R5.3}$$

$$3\,FeO + CO_2 \leftrightarrow Fe_3O_4 + CO \tag{R5.4}$$

The contribution of these two reactions for the CO production in the capture phase requires further research. Furthermore, H_2O production takes place in the capture phase as seen in Figure 5.11. This indicates that further reduction of the iron occurs [37].

During the He-flush no significant production of CO or CO_2 is detected. This confirms that the species responsible for CO_2 capture are strongly adsorbed on the catalyst surface. In analogy with the Cu-K system, the CO production in the reduction phase can be attributed to the decomposition of the produced carbonates (Reaction R5.2). Different compared to the previously discussed Cu-K/γ-Al_2O_3 is the immediate H_2O production in the reduction phase. This indicates that besides the decomposition of produced carbonates other reactions paths are present.

The immediate H_2O production can be attributed to the reduction of Fe_2O_3 into Fe_3O_4 (Reaction R5.5) as well as further reduction of Fe_3O_4 into FeO (Reaction R5.6). Besides the immediate water production, decomposition of formates into CO and H_2O can take place. The contributions of these reaction paths would require investigation of the surface species dynamics.

$$3\,Fe_2O_3 + H_2 \leftrightarrow 2\,Fe_3O_4 + H_2O \tag{R5.5}$$

$$Fe_3O_4 + H_2 \leftrightarrow 3\,FeO + H_2O \tag{R5.6}$$

During the reduction phase the produced CO can further react via reactions R5.3 and R5.4 and be converted into CO_2. This results in a product mixture consisting of a combination of CO and CO_2. The CO_2 capture capacity of this catalyst is 210 µmol g^{-1}. The CO production rate is comparable to the other catalysts with a value of 0.34 µmol g^{-1} s^{-1}. The molar ratio between CO and CO_2 in the product mixture is 3:1. Depending on the further processing of syngas, the presence of CO_2 can have an impact on the product distribution. One example is the use of the product mixture in the Fischer-Tropsch synthesis process. The process can utilize CO_2-rich syngas feeds, as long as the required catalytic activities such as the Fischer-Tropsch synthesis and water gas shift (WGS) reaction can occur [38]. If a catalyst is used with a low WGS activity, the product distribution will be toward smaller hydrocarbon chains e.g. methane [38].

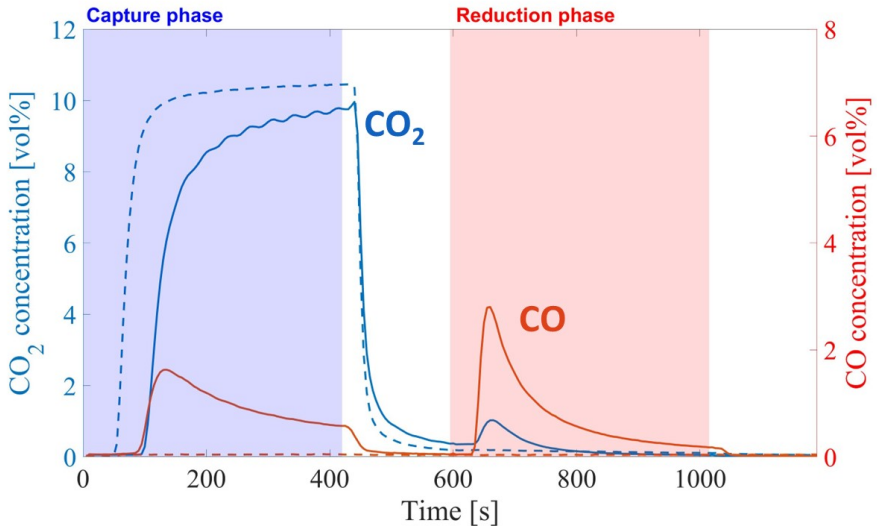

Figure 5.10: Catalytic behaviour of FeCrCuK/PMG20 at 450 °C. During the experiment flows of CO_2 of 15 mL min^{-1}, H_2 of 15 mL min^{-1} and a He-flush of 30 mL min^{-1} are used. The duration of the capture and reduction phase is 420 seconds, the He-flush phase is 175 seconds.

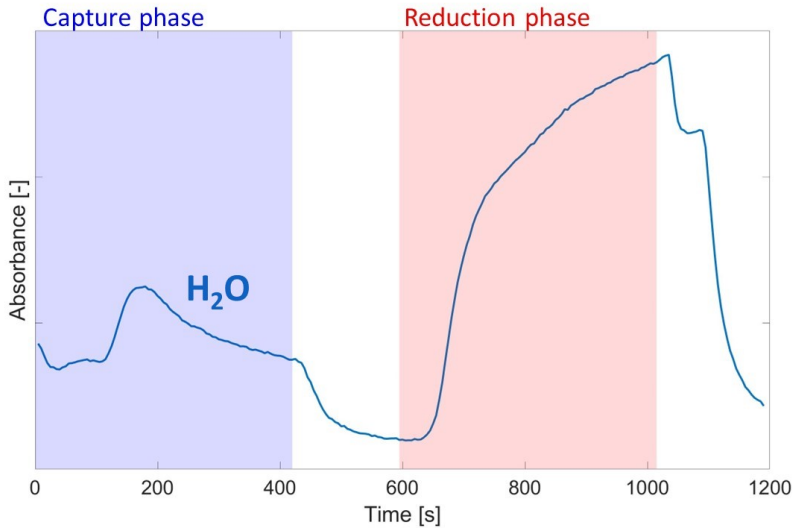

Figure 5.11: H_2O profile of FeCrCuK/PMG20 at 450 °C. During the experiment flows of CO_2 of 15 mL min^{-1}, H_2 of 15 mL min^{-1} and a He-flush of 30 mL min^{-1} are used. The duration of the capture and reduction phase is 420 seconds, the He-flush phase is 175 seconds.

Catalyst Selection

Based on the previously discussed results, it was decided to use Cu-K/γ-Al_2O_3 type 1 in the techno-economical analysis. It shows the highest CO_2 capacity, the highest CO production rate, and has a high selectivity to CO. Furthermore, in FeCrCuK/PMG20, H_2O production occurs immediately after switching to a H_2 environment and a significant amount of CO_2 is released in the reduction phase. If Cu-K/γ-Al_2O_3 is used, no H_2O production occurs during the fast reduction to CO. This is a favourable condition for process operations. The initial high release of CO in the reduction phase leads to a shorter period required for Cu-K/γ-Al_2O_3 compared to FeCrCuK/PMG20. When the CO production occurs slower, the operation requires a longer reduction duration. Consequently more H_2 is needed throughout the operation.

The CO_2 capacity, and CO production rate can be optimized further by utilizing different flow rates, concentrations, and capture and reduction phase duration. The optimization of the process depends on the amount of catalyst, as well as the installation the process will be attached to. In the techno-economical analysis the values obtained from the experiments with a shorter capture and reduction phase is used (see Figure 5.8) .

5.3. Hydrogen Quantification Results

This section describes the results of the H_2 quantification following the protocol reported in Section 3.5. First of all, the response obtained from the MS is visualized for the calibrations, the blank measurement and the experiment. Secondly, the resulting H_2 consumption is discussed. To obtain the ratio between the captured CO_2 and the consumed H_2 the IR alpha is used to determine the captured CO_2.

The H_2 quantification is performed for Cu-K/γ-Al_2O_3 catalyst type 1 and 2. As discussed in the protocol, the blank measurement is executed, followed by the calibration of this measurement. After bringing the reactor to 450 °C, the calibration of the experiment is performed, followed by the experiment itself. Figure 5.12 shows the profile of the H_2 ion current (m/z = 2).

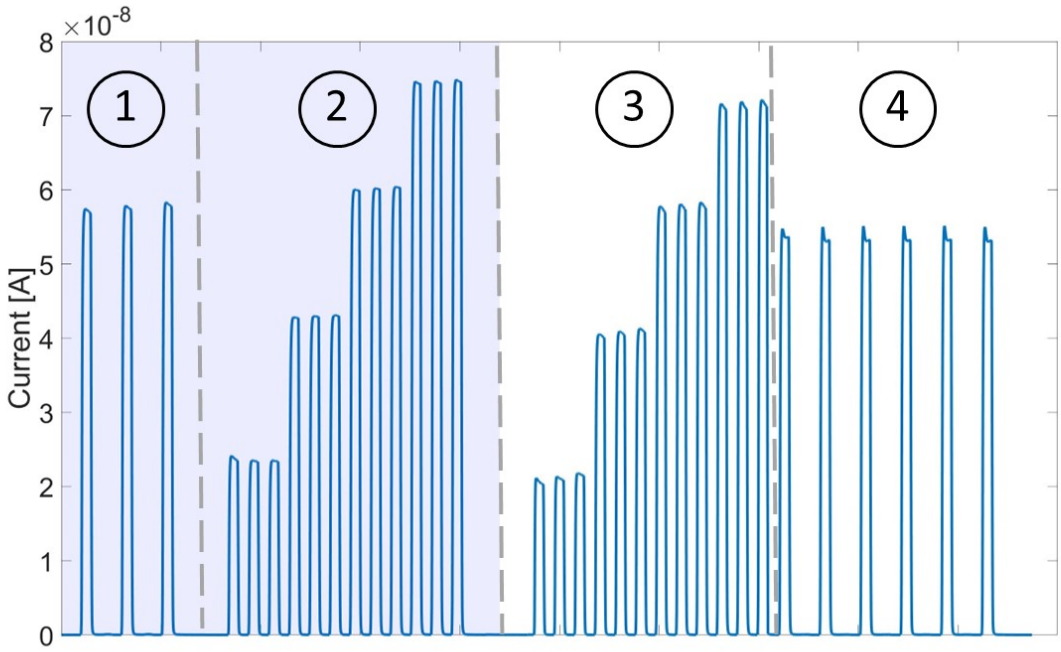

Figure 5.12: Ion current profile (m/z = 2) of 200 mg of Cu-K/γ-Al_2O_3 type 1 during the H_2 quantification experiment. Area indication: (1) blank measurement, (2) blank calibration, (3) experiment calibration and (4) experiment.

From this figure, it is clear that the signal is stable through the pulses. This ensures the reproducibility of the quantification. The first three pulses in the blue area represent the ion current from the blank measurement. To calibrate these pulses, the amount of H_2 is calculated using the calibration obtained from pulses 4 - 15 (area 2). The calibration curve for the blank measurement is visualized in Figure B.6 in Appendix B. Using this calibration curve the amount of H_2 through the blank measurement is calculated, which results in an average value of 40.7 mL.

To calculate the amount of H_2 during the experiment at 450 °C, a second calibration curve is obtained using pulses 16 - 27 (area 3). This calibration curve is visualized in Appendix B. Based on this calibration curve, the current caused by the H_2 during the experiment is converted into mL. As mentioned previously, the average of the last five cycles is taken due to divergent behaviour by the first cycle during the experiment. This results in a H_2 amount of 39.5 mL.

As mentioned in Section 3.3.2, the difference between the blank measurement and the experiment can be attributed to the consumption of H_2. Based on the previous mentioned values, the H_2 consumption during an experiment is 1.2 mL when 200 mg of catalyst is used. To determine the hourly flow of H_2 for the techno-economical analysis, the H_2 consumption in comparison to the captured CO_2 is determined.

The amount of CO_2 that is captured during this H_2 quantification is determined using the results from the IR alpha. A CO_2 capture of 27.7 µmol takes place during the capture phase. The consumption of H_2 during the

experiment is 47.5 µmol. Based on these values it is stated that per mol of CO_2 captured, 1.7 mol of H_2 is needed to convert the CO_2 into CO. The consumption of H_2 is higher than 1 mol expected from the reverse water gas shift reaction or the decomposition of carbonates formed during CO_2 capture. This difference is to an extent caused by the production of formates and activation of H_2 to form adsorbed species.

The previously discussed values are obtained utilizing Cu-K/γ-Al_2O_3 type 1 as bi-functional catalyst. To ensure the reproducibility of this protocol, the quantification is executed a second time using the same catalyst. This results in the same molar ratio between CO_2 and H_2, which shows that this protocol is reproducible. Furthermore, to determine whether the drying of the catalyst has an impact on the H_2 consumption, the same quantification is performed using Cu-K/γ-Al_2O_3 type 2. For the type 2 catalyst, the same ratio is found between the captured CO_2 and consumed H_2. This may indicate that the nature of the catalytic reaction is not modified by the different synthesis method.

Using the experimentally obtained value of H_2 amount, it is possible to determine the H_2/CO ratio of the syngas. To calculate the H_2/CO ratio, the FT-IR spectrometer is utilized to determine the amount of CO and CO_2 present during the reduction phase. This results in a H_2/CO, which is undesirable for downstream processing. The H_2/CO ratio is high due to the amount of catalyst and the large excess of H_2 utilized in this experiment.

To reduce the H_2/CO ratio to a usable value these parameters can be fluctuated. By increasing the amount of catalyst more CO_2 capture occurs, and subsequently, more CO production. Figure B.5 shows that it is possible to obtain full capture of CO_2 and an increase of CO production by simply increasing the amount of catalyst employed.

Furthermore, due to the developed protocol, the ratio between consumed H_2 and captured CO_2 is known. Taking this ratio into account the flow of H_2 can be fine tuned during process optimization. To optimize the flow of H_2 further, the reduction phase duration can be reduced. From the experiment as discussed in Section 5.2, it can be stated that most CO production occurs during the first 150 seconds of the reduction phase, after which limited amounts of CO are produced. By shortening the reduction phase, the focus is on the fast release of CO, consequently less H_2 is required. So during the process optimization the flow of gasses, duration of the capture and reduction phase, and amount of catalyst are parameters that can be altered. It is of importance that the capture phase ends before saturation of the active capture sites. The amount of catalyst will be determined by the CO_2 concentration in the flue gas and the supply of flue gas.

6

Techno-Economical Analysis

This chapter discusses the techno-economical analysis of the CCR process. Section 6.1 discusses the proposed process flow diagram (PFD) for the base-case scenario, and the capacity and size of the process equipment. Section 6.2 contains the economic analysis for the capital and operating costs as well as the profitability of the process.

6.1. Process Flow Diagram

Figure 6.1 shows the PFD. To evaluate the potential of the process, the equipment is reduced to its major components; additional equipment, valves, pressure controllers, and other safety devices, are not included. Once the CCR process is positively assessed, a more detailed PFD should be designed. For this analysis, two reactors are utilized, being the minimum, to ensure continuous operation. One reactor captures the CO_2 from flue gas, the other regenerates the catalyst in H_2 and produces syngas. In this analysis it is assumed that the capture and reduction phase are of equal duration, allowing for an even amount of reactors to be utilized.

Theoretically there is no limitation in the number of reactors that can be employed. Importantly, at more advanced stages of the analysis, the optimization of the CCR conditions and process configuration must be closely linked to the requirements of the upstream and downstream processes. The versatility of the CCR process permits adaptation to a wide range of conditions and external constrains. These include, but are not limited to; the CO_2 concentration in the flue gas source, the feed rate, the size of the reactors, and the temperature of the streams.

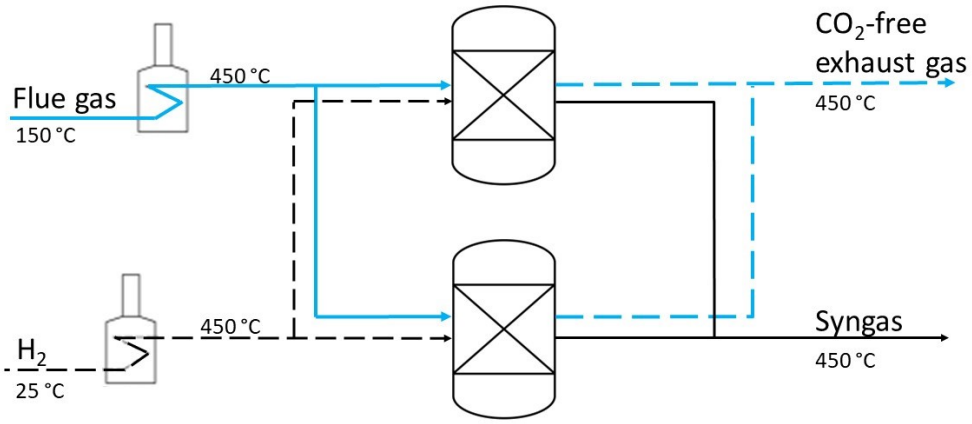

Figure 6.1: The process flow diagram of the CCR process using an inflow of H_2 and a flue gas which consists of 10 vol% CO_2 and the remainder N_2.

There are two streams that alternately flow into the packed bed reactor; the flue gas and H_2. In this analysis it is assumed that the flue gas consists of N_2 and CO_2, and that the concentration of CO_2 is 10 vol%. The inflow of CO_2 into the reactor is 660 kg/hr. This results in an inflow of 5,228 tonnes CO_2 per year assuming 330 days of operation. Based on the concentration of CO_2, the total mass flow of flue gas is determined. This results in a yearly flow of 35,116 tonnes.

The amount of catalyst determines the size of the reactors and, consequently, the amount of CO_2 that can be captured. From experimental evidences, it is assumed that the reduction can take place with a 100% conversion rate, and that the catalytic system can approach 100% capture of CO_2 [12]. During the capture no CO_2 or CO is detected (see Section 5.2). During the reduction phase, the active phase is regenerated to ensure CO_2 capture during the next capture phase. Previous research shows that the catalyst is stable over longer periods and that no CO_2 accumulation occurs on the catalyst surface [12, 33].

In the scenario of 100% capture of CO_2 and selective conversion to CO, the yearly CO production is 3,228 tonnes. Based on the experiment shown in Figure 5.8, the rate of CO production is taken as 0.78 $\mu mol\, g^{-1}\, s^{-1}$. The amount of catalyst required in a single reactor for the corresponding CO production is therefore 5,377 kg.

Based on the amount of catalyst and its density, the volume of the reactor is calculated. This results in a reactor volume of 10.8 m^3. The reactor height and width is determined by taking the aspect ratio into account. These values lead to a reactor with a diameter of 1.7 m and a height of 5 m, which is able to convert 5228 tonnes of CO_2 into CO. During the present analysis, it is assumed that the capture and reduction phase are of equal duration. This means that two reactors with the previously identified specifics are implemented to achieve continuous operation.

Parallel to the inflow of CO_2 into one reactor, an inflow of H_2 is required into the other reactor to reduce the captured CO_2 into CO. To directly obtain a valuable syngas at the reactor outlet, the H_2 inflow is set accordingly, taking into account the consumption of H_2 during the reaction. As mentioned previously in Section 2.2, a syngas ratio of two is required so that the syngas can be utilized for further processing e.g. methanol synthesis. In Section 5.3 it is determined that per mol of captured CO_2, 1.7 mol of H_2 is consumed during the reduction. Based on these two demands it is determined that the H_2 inflow is 905 tonnes per year, based on 330 days of operation.

The flue gas and H_2 need to be heated to 450 °C for process operation. A temperature of 450 °C is taken due to the higher CO_2 capacity and faster CO reduction rate compared to lower temperatures [35, 36]. Previous research shows that a small rise in temperature (ca. 4 °C) occurs during the capture phase, and a small temperature increase (ca. 0.5 °C) during the reduction phase [35]. This means that a part of the heat loss occurring due to the interaction of the reactor with the environment is temporarily compensated by the increase in temperature during the reaction. The heat loss to the environment is uncertain in this first analysis, therefore, it is assumed that the temperature in the reactor remains constant. Due to this assumption, it is sufficient to heat up the inflow gasses to the reaction temperature of 450 °C.

The temperature of inflow flue gas is taken as 150 °C as that is the temperature of the flue gas to the stack [39]. Contaminants such as SO_X, NO_X and particulate matter have already been removed [39]. The flue gas is heated to 450 °C, and based on a heuristic mentioned in the *Product and Process Design Principles* book the flue gas is heated using a fired heater [28]. The utility of this fired heater is determined using Aspen Plus V12 and results in a fired heater with a utility of 1.35 MMBtu/hr.

H_2 flow into the process is assumed to be at 25 °C. Based on the previously mentioned heuristic, a fired heater is also utilized for heating up the H_2 to 450 °C. According to Aspen Plus V12, the utility needed to heat up the H_2 is 0.67 MMBtu/hr. If H_2 is produced on location or obtained from another source, it is possible to have an inflow with a higher temperature. This reduces the requirement for heating H_2. Both the flue gas and the H_2 are at atmospheric pressure when entering the fired heaters. The assumption is made that no pressure drop occurs in the fired heaters.

After the gasses are heated using the fired heaters, they enter the packed bed reactor. Valves are used to cyclically alternate the gas feeds between the reactors, but the cost and technical aspects of these valves are not taken into account in this analysis. During the capture phase of a reactor, CO_2-free exhaust gas is flowing out of the reactor at a temperature of 450 °C. When the reactor is in the reduction phase, the outflow is syngas with a temperature of 450 °C and atmospheric pressure. Due to the many possibilities for syngas utilization, the post processing of the obtained syngas is outside the scope of this analysis.

Depending on the installation that the CCR process is attached to, a decision can be made regarding the utilization of the waste heat obtained from the flue gas and the CO_2-free exhaust gas. It is possible to use the waste heat in the installation that the CCR process is attached to or it can be utilized in the CCR process itself. The location of the utilization of the waste heat is determined by the company by a cost-benefit analysis. For example, it is possible to use the waste heat to pre-heat the flue gas and the H_2 before they enter the fired heaters. This solution can reduce the capital cost and partly compensate the cost of the fired heaters, as well as reducing the cost for utilities. This ensures that there is a level of adaptability for the optimization of the process and the installation it is attached to. The use of the waste heat is not taken into account in the present analysis.

6.2. Economics of the CCR Process

In this section the theoretical principles of the economics, as discussed in Section 3.6, are used to calculate the economics of the process. The analysis is based on the PFD discussed in the previous section.

6.2.1. Capital Costs

From the definition of the capital cost introduced in Section 3.6 and the total bare-module cost, an estimate is made for other costs: buildings, off-site facilities and land. The total bare-module cost of this process is estimated by the costs of the two reactors and the two fired heaters. To calculate the bare-module cost of the equipment, the purchase cost at a certain cost index and equipment size is determined.

Total Bare-Module Costs

The bare-module cost of a reactor is readily determined for a reactor of known diameter, height, and minimum wall thickness (5/16 inch). In Section 6.1 the sizing of the reactor is calculated and results in a diameter of 1.7 m, and a height of 5 m. Using the equations stated in Section 3.6, the cost of the empty vessel is \$26,316 at a CE index of 500. The purchase cost includes an allowance for platforms, ladders, and a nominal number of nozzles and manholes based on the diameter and length of the reactor. In this process those costs are estimated to be \$9,318. The assumption is made that no trays are present inside the reactor and that the reactor is constructed using carbon steel [40]. By utilizing these values in equation 3.9 the purchase cost of one reactor is \$35,634.

The bare-module factor of Guthrie for a vertical reactor is 4.16, and the pressure and material factors are 1 [28, 30]. If equation 3.6 is utilized the bare-module cost for one reactor is \$176,700, this does not include the cost of the catalyst.

This analysis assumes that the catalyst has the same lifetime as the reactor, this means that the catalyst cost is included in the capital costs. Previous research shows that a good stability is obtained for at least 50 CCR cycles utilizing Cu-K/γ-Al_2O_3 [33]. The catalyst was found to be stable under these conditions, showing that no CO_2 accumulation occurs on the catalyst surface. It is likely that the catalyst needs to be replaced during the lifetime of the reactor. Further research is required to determine the exact lifetime of the catalyst. If the lifetime is known, the catalyst cost can be included in the operating costs instead of in the captial costs. To determine the cost of the catalyst the methodology of Baddour et al. is used [41]. Appendix C shows the catalyst cost determination. The catalyst cost is approximated as \$27,129 per reactor, therefore the bare-module cost per reactor is \$203,829.

Besides the reactors, two fired heaters are required. The purchase cost of a fired heater is based on its utility per equations 3.7 and 3.8. The utility to heat up the flue gas from 150 °C to 450 °C is 1.35 MMBtu/hr, this results in a purchase cost of \$96,017 at a CE index of 500. Using the bare-module factor of Guthrie for a fired heater (2.16), the bare-module cost of this fired heater is \$250,651 after compensating for the CE index [28, 30]. In order to heat up the H_2 a utility of 0.67 MMbtu/hr is supplied, this results in a purchase cost of \$55,994. After multiplication with the bare-module factor and compensating for the CE index, the bare-module cost of this fired heat is \$146,172. Clearly, the cost of the fired heater for the flue gas is higher due to the higher amount of gas flowing through the heater.

The total bare-module cost is calculated by adding up all the previously mentioned bare-module costs, this results in a total bare-module cost of \$804,480.

Total Capital Investment

As mentioned in Section 3.6 the total capital investment consists of the total permanent investment and the working capital. The total permanent investment is calculated by adding the cost of land, buildings, and off-site facilities to the previously calculated total bare-module cost. The cost of land, buildings, and off-site facilities are responsible for $120,676 of the total capital investment. This leads to a total permanent investment cost of $925,152 when taking the contingency and contractor's fee into account.

The working capital is estimated to be 17.6% of the permanent investment, which is $162,827. This results in a total capital investment of $1,254,507.

The relative contribution of the different factors is illustrated in Figure 6.2. The total bare-module cost accounts for 64% of the total capital investment. This investment is divided equally between the cost of the two fired heaters, and the cost of the reactors and the catalyst. The contingency & contractor's fee account for 14% of the total capital investment. Less than 10% of the capital investment is attributed to site preparations, buildings, and offsite facilities.

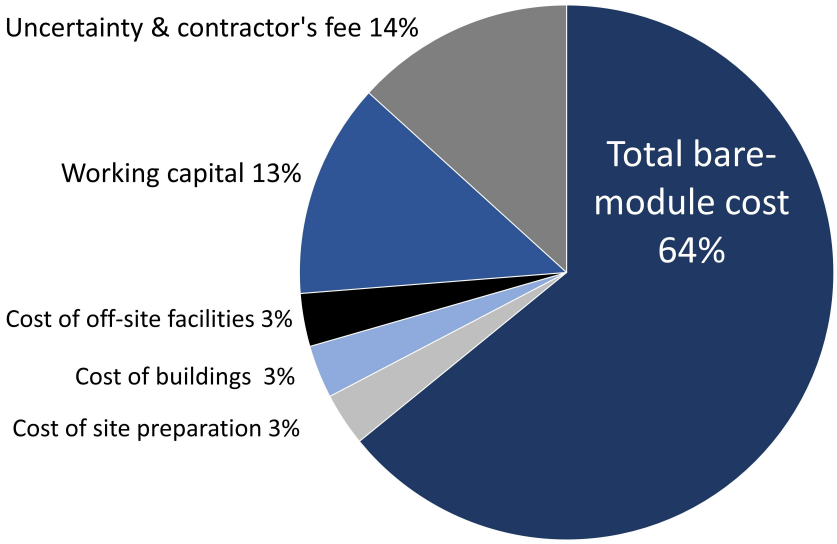

Figure 6.2: Relative contribution of different cost factors to the total capital investment for the CCR process.

6.2.2. Operating Costs

This section shows the economic analysis of the operating costs. The operating costs are separated into two groups: the feedstock costs, and ancillary costs. The ancillary costs include: utilities, maintenance, fixed costs, and general expenses.

Feedstock Cost

There are two feedstocks present in the CCR process: H_2, and flue gas. For this analysis it is assumed that the flue gas does not have an economical impact. To obtain a H_2/CO ratio in the syngas of 2, the flow of H_2 is 905 tonnes per year as discussed in Section 6.1. As mentioned in Section 2.3, a variety of processes are available for the production and supply of H_2. Due to its current availability, grey H_2 is utilized in this analysis, the buying price is estimated to be $1.5 per kilogram [42]. This results in a yearly cost of feedstock of $1,249,214.

Ancillary Costs

Besides the previously discussed feedstock there are other factors related to the operating costs. The first of the ancillary costs is the one attributed to the utilities as a result of heating the flue gas and H_2 before they flow into the reactors. The cost for the utilities is based on the calculated utility as found in Section 6.1. In this process a fired heater is employed to heat the gasses with a thermal efficiency of 85-90% [43]. To calculate the required flow of fuel for the fired heaters, an efficiency of 90% is used. In this analysis it is chosen to use natural gas as fuel in the fired heaters, considering a price of $0.175 per m^3 [44]. The yearly costs to heat

up the flue gas and H_2 are \$27,557 and \$55,717 respectively. These values are based on a required natural gas consumption of 19.9 $m^3\,h^{-1}$ and 40.2 $m^3\,h^{-1}$ respectively. This results in a total yearly cost for utilities of \$83,275.

As shown in Section 3.6.2 the maintenance is estimated to be 11.5% of the total depreciable capital, and leads to an annual maintenance cost of \$48,522. The property tax and insurance results in a yearly cost of \$32,348. The depreciation is estimated as 6.7% of the total depreciable cost, and results in a yearly cost of \$61,923.

The general expenses are estimated to be 9.55% of the yearly sales. In this analysis the yearly sales is determined by the produced syngas assumed to have a selling price of \$0.238 m^{-3} [45]. As mentioned in Section 6.1, the syngas production is 3,826 tonnes per year. This results in a yearly sale revenue of \$1,949,336, and subsequently a yearly general expense of \$186,162.

Total Production Cost

The total production cost of this CCR process is \$1,661,443. This is mainly caused by the cost of H_2 in the feedstock, as seen in Figure 6.3. The remaining 24% is attributed to the ancillary costs such as the general expenses.

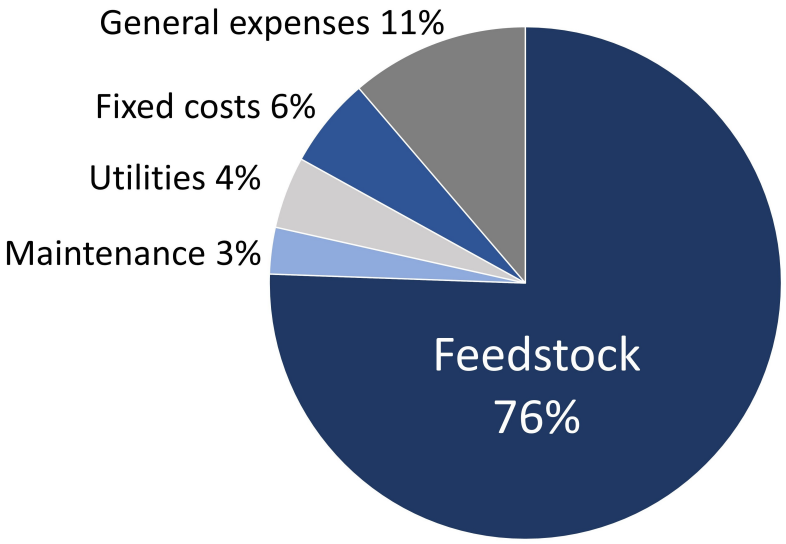

Figure 6.3: Relative contribution of different cost factors to the total production cost of the CCR process.

6.2.3. Profitability Analysis

The gross earnings of the CCR process is determined by subtracting the total operating cost from the yearly revenue, \$1,949,336 and \$1,661,443 respectively. The yearly gross earnings of this process before tax is \$287,893. After tax this results in a yearly net earning of \$215,920.

The previously mentioned yearly net earning does not take into account potential profits obtained from selling allowances present in the cap-and-trade system. If the installation the CCR process is attached to, is located within a country with a policy in place with an auction for CO_2 emission allowances, a higher profit can be obtained. Assuming the installation and the CCR process is located in the European Union, the EU ETS would be in place (see Chapter 2). Based on the sector and the efficiency of the installation, free allowance can be allocated to the company.

If no free allowances are obtained as a results of an inefficient installation, the yearly net earnings remain \$215,920. If the installation is efficient and is in a sector with potential carbon leakage, the installation can receive allowances for 5,228 tonnes of CO_2. By having a carbon neutral process, the received allowances can be auctioned to a different company. This means that the profitability of the process itself is increased

significantly. Assuming a carbon price of €80 per tonne of CO_2, an additional yearly profit of $460,064 is obtained. This increases the yearly profit of the process itself to $675,984.

So the yearly net earnings are between $215,920 and $675,984 depending on the sector in which the installation is present as well as the efficiency of the installation.

As discussed in Section 3.6, large net earnings may not be sufficient if it is not possible to payback the original investment. With a yearly profit of $215,920, the payback period is 3.3 years. This period is substantially reduced in the emission trading scheme, where the yearly profit of $675,984 allows full payback of the investment in 1.2 years. The additional profit can be utilized to reduce the payback period of the CCR process. It is unlikely that companies invest in projects with a payback period of more than four years due to the rapid progress in technology [28]. Since the payback period ranges between 1.2 and 3.3 years, the CCR process exhibits potential as a technology to reduce the CO_2 emissions of existing facilities.

6.3. Source of H_2

As mentioned previously, the type of H_2 utilized in the economical analysis is grey H_2. The production of grey H_2, mainly reliant on steam methane reforming, emits a significant amount of CO_2, ca. 9.3 kg CO_2 per kg H_2 [24]. For the parameters investigated for the CCR process, the employment of grey H_2 will result in a yearly emission of 9,048 tonnes of CO_2. Yearly only 5,228 tonnes of CO_2 is captured, resulting in a non-carbon neutral process. To achieve net zero CO_2 emission or a negative carbon footprint, a different H_2 source needs to be used.

One possibility is to attach the CCR process to a grey H_2 production plant, such as the steam methane reforming process. The H_2 produced by this installation can be used in the CCR while the CO_2 emitted from the installation is captured by the CCR process. This means that the H_2 produced by the production plant becomes 'blue' H_2, since the CO_2 generated is not emitted to the atmosphere, but rather captured and converted by the CCR reactors. In this perspective, the CCR process can be seen not only as a CO_2 capture and utilisation strategy, but also as a technology for H_2 production with a reduced carbon footprint. This can potentially increase the value and market price of the produced H_2.

Alternatively, it is possible to use blue H_2 that utilizes a different capture technology. The employment of blue H_2 is still associated with a carbon footprint, however less CO_2 emissions occur compared to the production of grey H_2. Per kilogram of H_2, 0.82-2.55 kilograms of CO_2 are emitted during the production of blue H_2 [46]. This means that depending on the production method, 742 - 2,307 tonnes of CO_2 is emitted during the H_2 production for the CCR process. In this context, the amount of CO_2 captured in the CCR process is higher than the CO_2 emitted by H_2 production. This ensures that the process has a positive impact on the reduction of CO_2 emissions. The price of blue H_2 is in the same order of magnitude of grey H_2. According to Yu et al., the production cost of blue H_2 is in the range of 0.99 and 2.05 \$/kgH_2, while the IRENA specifies a cost of H_2 between 1.2 and 2.3 \$/kgH_2 [47, 23]. The buying price of H_2 would be higher if it is obtained from a different installation and transported to the CCR process.

However, CO_2 emissions still occur if blue H_2 is used in the CCR process. The use of green H_2 in the process would improve the impact the CCR process has on the CO_2 emissions, since no emissions occur during the production. Currently, the cost of green H_2 is two to three times higher than the cost of grey H_2 [48]. The price of green H_2 is dependent on the location it is produced as seen in Figure 6.4. For example, the price of green H_2 is 2.2 \$/kgH_2 in Australia, and around 4 \$/kgH_2 in other parts of the world in the year 2020.

As illustrated in Figure 6.3, the H_2 has a large impact on the operating cost of the process, and consequently, on the net earnings. Figure 6.5 shows the impact of the H_2 price on the net earnings. If the sales of allowances in the EU are taken into account the process remains profitable up to a H_2 price of 2.4 \$/kgH_2. If the sales of allowances are not taken into account, the process is profitable up to a H_2 price of 1.8 \$/kgH_2. In countries such as Mexico and Chile only a carbon tax is implemented. This means that the profitability is not dependent on the sales of allowances.

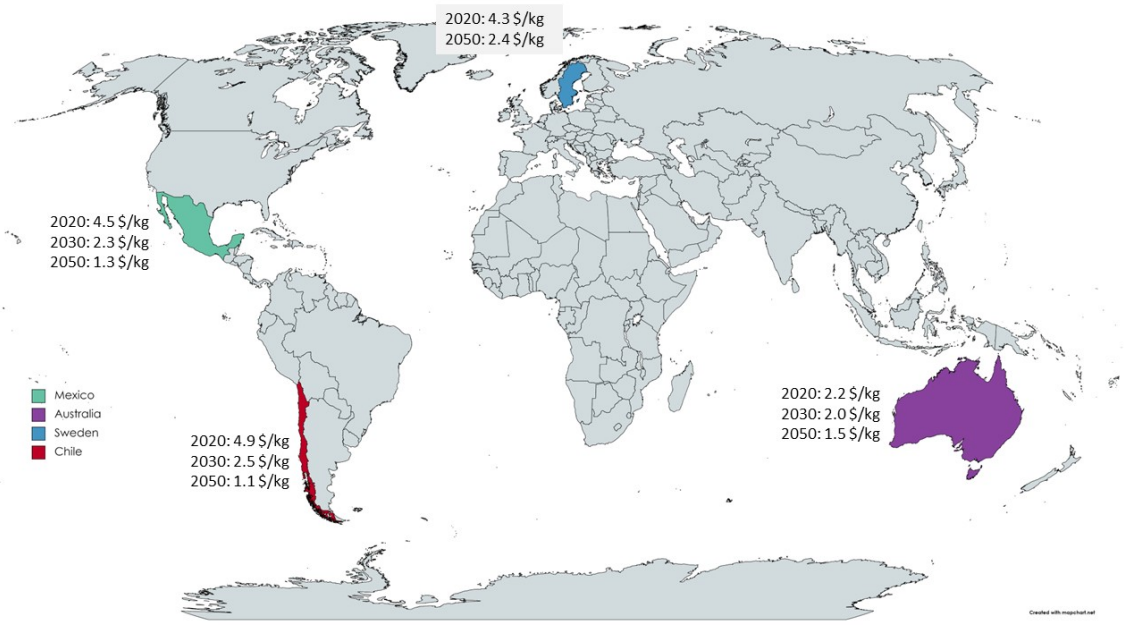

Figure 6.4: Green H_2 price for different locations and different years. Values obtained from: [49, 50, 51, 52]

The area in which a profit is made is the shaded area in Figure 6.5. If the price of H_2 of the chosen source is above \$2.4/kgH_2, the CCR process is not profitable in the current energy infrastructure in the EU. This means that the price corresponding to green H_2 is too high in certain locations to be economically viable even considering the aforementioned scenario with selling of the emission allowances. However, the future trends on the energy transition will assist in lowering the price of green H_2 as seen in Figure 6.4.

With the current infrastructure and H_2 production methods, it is concluded that it is more beneficial to utilize blue H_2 in the CCR process in the EU. However, as soon as the cost of green H_2 is lower or similar to blue/grey H_2, it is recommended to be used to substantially increase the impact the CCR process has on the CO_2 emissions.

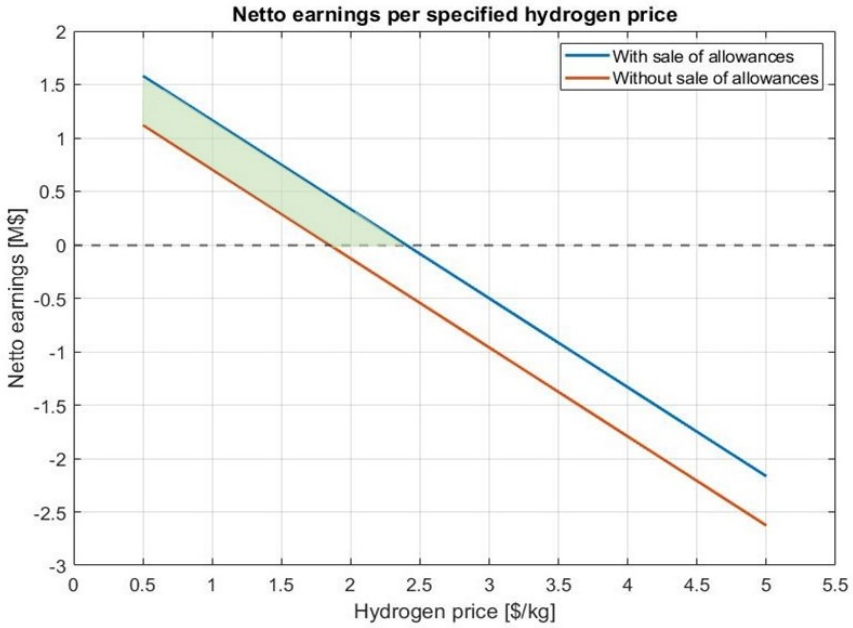

Figure 6.5: Impact of the H_2 price on the netto earnings of the CCR process.

7

Conclusion and Recommendations

The objective of this work was to determine the economical feasibility of the CCR process, combining experimental knowledge on the catalytic system with the evaluation of the techno-economics of a continuous process operation.

In the first part of the experimental work, three catalysts were synthesised using the incipient wetness impregnation method. Two catalysts consisted of K-promoted Cu/γ-Al_2O_3 prepared with standard wetness impregnation (type 1) and with a modified synthesis including controlled drying of the support before impregnation (type 2). The third catalyst that has been synthesised consists of a mixture of active metals (Fe, Cr and Cu) and K impregnated on a hydrotalcite support (PMG20).

To determine the best candidate for the techno-economic analysis, a catalyst screening protocol was developed to obtain a method to determine the CO_2 capacity of the catalyst. To quickly screen the catalyst, the TGA was utilized to observe the weight change occurring in the presence of CO_2. The weight change difference between the CO_2/H_2 and CO_2/N_2 experiments represents the CO_2 capacity of the catalyst as observed in the reactor setup. During the switching between CO_2 and N_2, a weight change was observed which requires further research. Based on the obtained results and the uncertainty surrounding the occurring weight change, the CO_2 capacity of the catalyst is determined using the reactor setup.

In the reactor setup, three catalyst have been tested to determine their CO_2 capacity and CO production rate. First, longer capture and reduction phase durations were used to analyze the occurring behaviour. From Cu-K/γ-Al_2O_3 it could be seen that most CO production occurs with a fast release in the first 150 seconds of the reduction phase. During this fast release, no release of H_2O takes place. During the tailing effect of the CO production of Cu-K/γ-Al_2O_3 a release of H_2O does occur. If FeCrCuK/PMG20 is used, an immediate H_2O generation is present when switching to a H_2 flow. Furthermore, unconverted CO_2 is released in the reaction phase. This results in a product composition consisting of a mixture of CO_2, CO, H_2O, and H_2 when using FeCrCuK/PMG20. The CO_2 capacity and CO production rate of Cu-K/γ-Al_2O_3 type 2 and FeCrCuK/PMG20 were lower than the Cu-K/γ-Al_2O_3 type 1. The difference between Cu-K/γ-Al_2O_3 type 1 and type 2 can be attributed to a difference in the catalyst loading. Based on the higher CO_2 capacity and faster CO production rate, Cu-K/γ-Al_2O_3 type 1 was selected as the catalyst in the techno-economical analysis. The values used in the analysis were based on experiments using a short capture and reduction phase duration of 150 seconds.

Before the techno-economical analysis was performed, a H_2 quantification protocol was developed and executed to determine the consumption of H_2. The consumption of H_2 is determined to obtain the H_2 inflow required to convert the captured CO_2 to CO and to obtain a product composition with a H_2/CO ratio of 2. The H_2 quantification was performed using the MS, while the FT-IR spectrometer was employed to quantify the captured CO_2 and determine the H_2 consumption per mol of CO_2 captured for Cu-K/γ-Al_2O_3. Based on the quantification, it is determined that per mol of CO_2 captured, 1.7 mol of H_2 is consumed. Due to the excess amount of H_2 utilized in the reactor setup, an undesirable H_2/CO is obtained. At industrial scale, optimization of the process operation parameters, such as the amount of catalyst and flowrate of the gasses, needs to be accomplished to obtain a valuable syngas.

To analyze the economical feasibility of the process, a PFD is developed utilizing the data obtained in the experimental part of this thesis. In the analysis a two-reactor type system is used to ensure a continuous operation. Based on the PFD and the inflow streams, the sizing of the two furnaces and two reactors was determined. Using these values, the capital costs of the process were estimated. Besides the capital costs of the process, also the yearly operating costs were determined. From the determination of the operating costs

it was clearly visible that the largest contribution to the cost is attributed to the used feedstock. When utilizing grey H_2 as a feedstock, a yearly net earnings of $215,920 can be achieved. If the installation the CCR is attached to is located in the EU and is efficient, the obtained free allowances can be sold for market value. This can increase the yearly net earnings to $675,984. When making use of grey H_2 in this process, a net zero CO_2 emission cannot be obtained. In order to obtain a net zero CO_2 emission, a different source of H_2 should be used. The sources that can be used are blue and green H_2, of which the latter has the preference. Currently, green H_2 is in most countries not yet price competitive with grey and blue H_2. As soon as the price of green H_2 is below 1.8 $/kg in a country, a profitable process is obtained without the sale of allowances. So, the process is profitable if the used H_2 source has a buying price below $1.8 per kilogram. If sales of allowances is possible, the buying price of H_2 needs to be below $2.4 to ensure a profitable process.

To conclude, the CCR process can add significant value to CO_2 present in flue gas. The diluted stream of CO_2 is fully captured and reduced into CO under a H_2 atmosphere. In the near future, the price of green H_2 will become price competitive with grey H_2 which shows the large potential of the CCR process.

7.1. Recommendations

The thesis, which benefited from a combined approach from chemical engineering and sustainable energy technology, highlighted interesting directions for the exploitation and industrialization of the CO_2 capture and reduction process. In this section recommendations are given for future research.

First of all, a protocol for fast catalyst screening employing TGA has been developed in this thesis. A weight change took place when switching between CO_2 and N_2, a weight change not observed in the reactor setup. To improve and verify the protocol, further research needs to address the cause of this weight change. One possibility is to analyze the outflow gasses with a MS in order to determine the composition. The outflow gasses of the same experiment in the reactor setup are analyzed as well. These compositions can be compared with each other to create a further understanding of the occurring behaviour. If the catalyst screening protocol has been verified and tested further, it can be utilized to test and develop more catalyst compositions. If the catalyst shows a promising CO_2 capacity, their catalytic behaviour can be tested in the reactor setup.

Secondly, during this thesis the feed to the reactor consisted of pure reactants diluted with an inert gas. Flue gas contains other gases such as O_2 or H_2O that can have an impact on the process operation. It would be insightful to test the influence on the CO_2 capture capacity and CO production rate, as well as the stability of the performance.

Furthermore, in most experiments a catalyst weight of 200 mg was utilized in the reactor setup. Currently, a larger catalyst bed has not been optimized, and a significant catalyst weight increase cannot be tested. If the setup is altered, and the catalyst bed can be increased significantly, the influence of the catalyst weight on the CO_2 capture capacity and CO production can be estimated. If this is verified, the knowledge obtained during lab scale process optimization can be used on a pilot scale. If a pilot scale operation is used, optimization of the process parameters can take place. An important process parameter to alter is the duration of the capture and reduction phase in relation to the flowrate of the gasses. In this thesis it was found that a fast release of CO occurs without the release of H_2O at the beginning of the reduction phase. However, sufficient regeneration of the catalyst should take place to ensure adequate active sites for CO_2 capture.

Moreover, the optimization of the process parameters can improve the level of detail of the PFD used in the techno-economical analysis. If a detailed plant design is known, the capital cost can be estimated with a higher level of accuracy. In addition, if the installation and its location is known where the CCR process will be attached to, the operational cost can be calculated with a higher certainty. If the location is known, the cost of feedstock and utilities can be determined for that specific location. Furthermore, the labor-related cost can be included based on the process requirements and location.

Bibliography

[1] C. Riedel, “Emissions rise from the smokestacks at the jeffrey energy center coal power plant as the suns sets,” 2021, http://www.apimages.com/metadata/Index/UN-Air-Quality/776fb5a2dd90491684381499985159 29/141/0.

[2] International Energy Agency, “Global energy review: CO_2 emissions in 2021,” 2021, https://www.iea.org/reports/global-energy-review-co2-emissions-in-2021-2.

[3] IPCC, “Summary for policymakers, technical summary and frequently asked questions,” 2013, https://www.ipcc.ch/site/assets/uploads/2018/03/WG1AR5_SummaryVolume_FINAL.pdf.

[4] M. Fischedick, J. Roy, A. Abdel-Aziz, A. Acquaye, J. Allwood, J.-P. Ceron, Y. Geng, H. Kheshgi, D. P. Alessandro Lanza (and, L. Price, E. Santalla, C. Sheinbaum, and K. Tanaka, “Climate change 2014: Mitigation of climate change,” 2014, https://www.ipcc.ch/site/assets/uploads/2018/02/ipcc_wg3_ar5_chapter10.pdf.

[5] S. D. Clara and K. Mayr, “The EU ETS phase IV reform: implications for system functioning and for the carbon price signal,” 2018, https://www.oxfordenergy.org/publications/eu-ets-phase-iv-reform-implications-system-functioning-carbon-price-signal/.

[6] A. Barnes, “The challenges and prospects for carbon pricing in europe,” 2021, https://www.oxfordenergy.org/publications/the-challenges-and-prospects-for-carbon-pricing-in-europe/.

[7] “Allocation to industrial installations,” https://ec.europa.eu/clima/eu-action/eu-emissions-trading-system-eu-ets/free-allocation/allocation-industrial-installations_en, accessed: 22-03-2022.

[8] European Commission, “Market stability reserve,” 2021, https://ec.europa.eu/clima/eu-action/eu-emissions-trading-system-eu-ets/market-stability-reserve_en.

[9] Trading Economics, “EU carbon permits,” 2021, https://tradingeconomics.com/commodity/carbon#:~:text=EU%20Carbon%20Permits%20is%20expected,83.74%20in%2012%20months%20time.

[10] T. Drage, C. Snape, L. Stevens, J. Wood, J. Wang, X. Guo, C. Cazorla Silva, R. Dawson, and A. Cooper, “Step change adsorbents and processes for CO_2 capture ”STEPCAP”,” *Abstracts of Papers of the American Chemical Society*, vol. 243, Mar. 2012, 11th International Biorelated Polymer Symposium / 243rd National Spring Meeting of the American-Chemical-Society (ACS) ; Conference date: 25-03-2012 Through 29-03-2012.

[11] IPCC, “IPCC special report on carbon dioxide capture and storage,” 2005.

[12] L. F. Bobadilla, J. M. Riesco-García, G. Penelás-Pérez, and A. Urakawa, “Enabling continuous capture and catalytic conversion of flue gas CO_2 to syngas in one process,” *Journal of CO2 Utilization*, vol. 14, pp. 106–111, 2016. [Online]. Available: https://www.sciencedirect.com/science/article/pii/S2212982016300312

[13] I. Ghiat and T. Al-Ansari, “A review of carbon capture and utilisation as a co2 abatement opportunity within the ewf nexus,” *Journal of CO_2 Utilization*, vol. 45, p. 101432, 2021. [Online]. Available: https://www.sciencedirect.com/science/article/pii/S2212982020310623

[14] S. Lin, T. Kiga, Y. Wang, and K. Nakayama, “Energy analysis of $CaCO_3$ calcination with CO_2 capture,” *Energy Procedia*, vol. 4, pp. 356–361, 2011, 10th International Conference on Greenhouse Gas Control Technologies. [Online]. Available: https://www.sciencedirect.com/science/article/pii/S1876610211000646

[15] F. Wu, M. D. Argyle, P. A. Dellenback, and M. Fan, “Progress in O_2 separation for oxy-fuel combustion–a promising way for cost-effective CO_2 capture: A review,” *Progress in Energy and Combustion*

Science, vol. 67, pp. 188–205, 2018. [Online]. Available: https://www.sciencedirect.com/science/article/pii/S0360128517300801

[16] C. Hepburn, E. Adlen, J. Beddington, E. Carter, S. Fuss, N. M. Dowll, J. Minx, P. Smith, and C. Williams, "The technological and economic prospects for CO_2 utilization and removal," *Nature*, vol. 575, pp. 87–97, 2019. [Online]. Available: https://doi.org/10.1038/s41586-019-1681-6

[17] T. Hyakutake, W. van Beek, and A. Urakawa, "Unravelling the nature, evolution and spatial gradients of active species and active sites in the catalyst bed of unpromoted and K/Ba-promoted Cu/Al_2O_3 during CO_2 capture-reduction," *J. Mater. Chem. A*, vol. 4, pp. 6878–6885, 2016. [Online]. Available: http://dx.doi.org/10.1039/C5TA09461E

[18] R. Prins, "On the structure of γ-Al_2O_3," *Journal of Catalysis*, vol. 392, pp. 336–346, 2020. [Online]. Available: https://www.sciencedirect.com/science/article/pii/S0021951720304164

[19] C.-Y. Chou, J. A. Loiland, and R. F. Lobo, "Reverse water-gas shift iron catalyst derived from magnetite," *Catalysts*, vol. 9, no. 9, 2019. [Online]. Available: https://www.mdpi.com/2073-4344/9/9/773

[20] S. A. Farooqui, A. K. Sinha, and A. Ray, "Chapter 13 - progress and trends in renewable jet fuels," in *Advanced Biofuel Technologies*, D. Tuli, S. Kasture, and A. Kuila, Eds. Elsevier, 2022, pp. 333–364. [Online]. Available: https://www.sciencedirect.com/science/article/pii/B9780323884273000118

[21] C. Yang, Z. Ma, N. Zhao, W. Wei, T. Hu, and Y. Sun, "Methanol synthesis from CO_2-rich syngas over a ZrO_2 doped cuzno catalyst," *Catalysis Today*, vol. 115, no. 1, pp. 222–227, 2006, proceedings of the 8th International Conference on Carbon Dioxide Utilization. [Online]. Available: https://www.sciencedirect.com/science/article/pii/S092058610600112X

[22] P. L. Spath and D. C. Dayton, "Preliminary screening – technical and economic assessment of synthesis gas to fuels and chemicals with emphasis on the potential for biomass-derived syngas," 12 2003. [Online]. Available: https://www.osti.gov/biblio/15006100

[23] IRENA, "Making the breakthrough: Green hydrogen policies and technology costs," 2021, https://www.irena.org/-/media/Files/IRENA/Agency/Publication/2020/Nov/IRENA_Green_Hydrogen_breakthrough_2021.pdf?la=en&hash=40FA5B8AD7AB1666EECBDE30EF458C45EE5A0AA6.

[24] R. Rapier, "Estimating the carbon footprint of hydrogen production," https://www.forbes.com/sites/rrapier/2020/06/06/estimating-the-carbon-footprint-of-hydrogen-production/?sh=30f6a41e24bd, accessed: 22-04-2022.

[25] D. Oudejans, M. Offidani, A. Constantinou, S. Albonetti, N. Dimitratos, and A. Bansode, "A comprehensive review on two-step thermochemical water splitting for hydrogen production in a redox cycle," *Energies*, vol. 15, no. 9, 2022. [Online]. Available: https://www.mdpi.com/1996-1073/15/9/3044

[26] T. inquisitive investor, "Green hydrogen: An investment for the future," 2021, https://medium.com/@TheInquisitiveInvestor/green-hydrogen-an-investment-for-the-future-c246e8a80c56.

[27] H. van Leeuwen, "The effects of synthesis conditions on the properties and performances of catalysts suitable for CO_2 capture and reduction processes," 2021.

[28] W. D. Seider, J. D. Seader, D. R. Lewin, and S. Widagdo, *PRODUCT & PROCESS DESIGN PRINCIPLES: synthesis, analysis and evaluation*. John Wiley & Sons, 2010.

[29] Chemical Engineering, "Economic indicators," 2021, https://ic.nipc.ir/ic/Portals/0/Introduce/cost%20index/May2021.pdf.

[30] M. van Amsterdam, "Factorial techniques applied in chemical plant cost estimation: A comparative study based on literature and cases," 2018.

[31] L. Fernándes-Carrasco, F. Puertas, M. T. Blanco-Varela, T. Vazques, and J. Rius, "Synthesis and crystal structure solution of potassium dawsonite : An intermediate compound in the alkaline hydrolysis of calcium aluminate cements," vol. 35, pp. 641–646, 2005. [Online]. Available: http://dx.doi.org/10.1016/j.cemconres.2004.04.018

[32] S. Walspurger, L. Boels, P. D. Cobden, G. D. Elzinga, W. G. Haije, and R. W. Van Den Brink, "The crucial role of the K+-aluminium oxide interaction in K +-promoted alumina-and hydrotalcite-based materials

for CO_2 sorption at high temperatures," *ChemSusChem*, vol. 1, no. 7, pp. 643–650, 2008. [Online]. Available: http://dx.doi.org/10.1002/cssc.200800085

[33] S. Minorello, "Investigation of isothermal unsteady-state CO_2 capture and reduction over k-promoted supported cu-catalysts," 2020.

[34] D. Pinto, V. van der Bom, and A. Urakawa, "Mechanistic insights into the CO_2 capture and reduction on K-promoted Cu/Al_2O_3 by spatiotemporal operando methodologies," submitted manuscript.

[35] V. van der Bom, "Expanding the horizons of CO_2 capture and reduction," 2021.

[36] Z. Zhou, "Carbon dioxide capture and reduction: influence of reaction conditions and potassium precursors on the catalytic activity development," 2021.

[37] C. Ratnasamy and J. P. Wagner, "Water gas shift catalysis," *Catalysis Reviews*, vol. 51, no. 3, pp. 325–440, 2009. [Online]. Available: https://doi.org/10.1080/01614940903048661

[38] O. O. James, A. M. Mesubi, T. C. Ako, and S. Maity, "Increasing carbon utilization in fischer–tropsch synthesis using h2-deficient or co2-rich syngas feeds," *Fuel Processing Technology*, vol. 91, no. 2, pp. 136–144, 2010. [Online]. Available: https://www.sciencedirect.com/science/article/pii/S037838200900294X

[39] C. Song and W. Pan, "Tri-reforming of methane: a novel concept for catalytic production of industrially useful synthesis gas with desired H_2/CO ratios," *Catalysis Today*, vol. 98, no. 4, pp. 463–484, 2004. [Online]. Available: https://www.sciencedirect.com/science/article/pii/S0920586104005644

[40] B. P. Somerday and C. S. Marchi, "Effects of hydrogen gas on steel vessels and pipelines," 2006, https://www.osti.gov/servlets/purl/1727338.

[41] F. G. Baddour, L. Snowden-Swan, J. D. Super, and K. M. Van Allsburg, "Estimating precommercial heterogeneous catalyst price: A simple step-based method," *Organic Process Research & Development*, vol. 22, no. 12, pp. 1599–1605, 2018. [Online]. Available: https://doi.org/10.1021/acs.oprd.8b00245

[42] E. Commission, "A hydrogen strategy for a climate-neutral europe'," 2020, https://ec.europa.eu/energy/sites/ener/files/hydrogen_strategy.pdf.

[43] "Waste heat recovery from fired heaters," https://heatmatrixgroup.com/thermal-processes/fired-heater/#:~:text=Fired%20Heaters%20are%20used%20in,around%2085%25%20%E2%80%93%2090%25., accessed: 05-04-2022.

[44] "Price of natural gas," https://markets.businessinsider.com/commodities/natural-gas-price, accessed: 22-03-2022.

[45] P. Zuldian, S. Fukuda, and M. Bustan, "Economic analysis of coal gasification plant for electricity and thermal energy supplies in indonesia," *Journal of Clean Energy Technologies*, vol. 5, pp. 193–198, 05 2017.

[46] L. van Cappellen, H. Croezen, and F. Rooijers, "Feasibility study into blue hydrogen," 2018, https://cedelft.eu/wp-content/uploads/sites/2/2021/04/CE_Delft_9901_Feasibility_study_into_blue_hydrogen_DEF_bak.pdf.

[47] M. Yu, K. Wang, and H. Vredenburg, "Insights into low-carbon hydrogen production methods: Green, blue and aqua hydrogen," *International Journal of Hydrogen Energy*, vol. 46, no. 41, pp. 21 261–21 273, 2021. [Online]. Available: https://www.sciencedirect.com/science/article/pii/S0360319921012684

[48] IRENA, "Green hydrogen: A guide to policy making," 2020, https://www.irena.org/-/media/Files/IRENA/Agency/Publication/2020/Nov/IRENA_Green_hydrogen_policy_2020.pdf.

[49] IEA, "Hidrógeno en américa latina. de las oportunidades a corto plazo al despliegue a gran escala," 2021, https://iea.blob.core.windows.net/assets/8bad1e39-1587-4770-b60a-c9368e6347ae/IEA_HydrogeninLatinAmerica_Fullreport_Spanish.pdf.

[50] HINICO, "Green hydrogen in mexico: towards a decarbonization of the economy," 2021, https://www.energypartnership.mx/fileadmin/user_upload/mexico/media_elements/reports/Hydrogen_EP_volume_VII.pdf.

[51] ICCT, "Cost of renewable hydrogen produced onsite at hydrogen refueling stations in europe," 2022, https://theicct.org/wp-content/uploads/2022/02/fuels-eu-cost-renew-H-produced-onsite-H-refueling-stations-europe-feb22.pdf.

[52] D. Carroll and B. Peacock, "Australian study labels green hydrogen cost projections as 'too conservative'," 2021, https://www.pv-magazine.com/2021/05/27/australian-study-labels-green-hydrogen-cost-projections-as-too-conservative/.

[53] "Price of γ-Al_2O_3," https://www.sigmaaldrich.com/NL/en/product/mm/101095, accessed: 24-03-2022.

[54] "Price of $CuNO_3$," https://www.sigmaaldrich.com/NL/en/product/mm/102753, accessed: 24-03-2022.

[55] "Price of K_2CO_3," https://www.sigmaaldrich.com/NL/en/product/aldrich/367877, accessed: 24-03-2022.

Appendices

A

N_2 Adsorption Plots

Figures A.1 and A.2 show the N_2 adsorption isotherm linear plots for different samples.

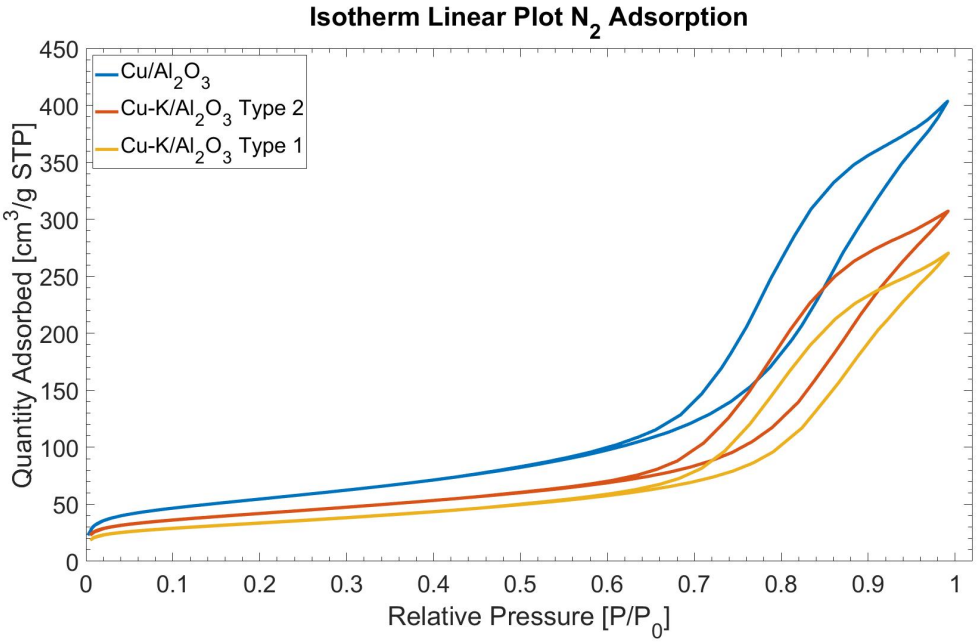

Figure A.1: The isotherm linear plot for Cu/γ-Al_2O_3, Cu-K/γ-Al_2O_3 type 1 and Cu-K/γ-Al_2O_3 type 2 obtained by N_2 adsorption.

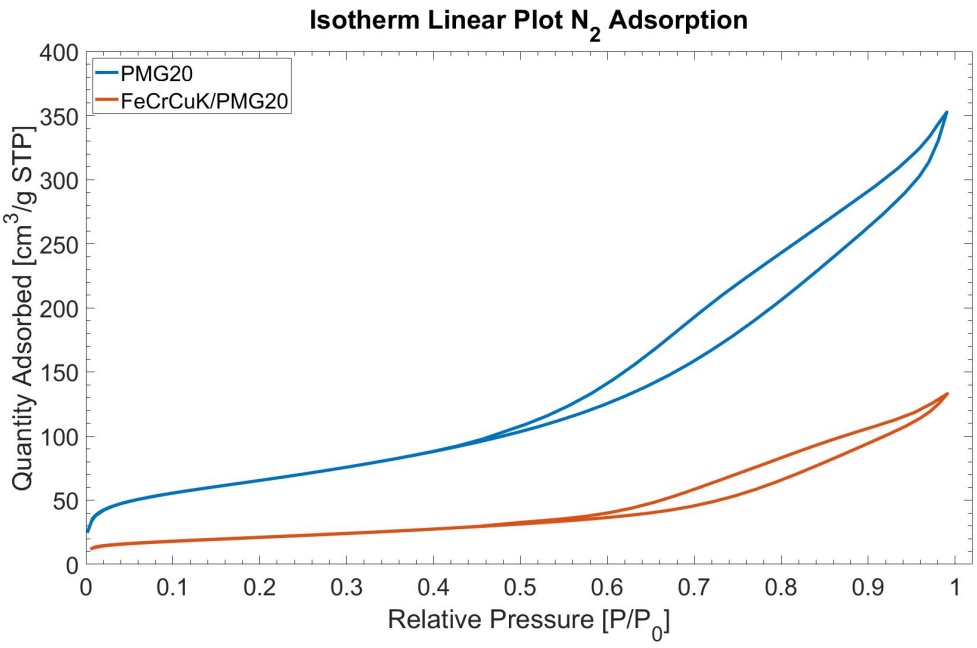

Figure A.2: The isotherm linear plot for PMG20 and FeCrCuK/PMG20 obtained by N_2 adsorption.

B

Additional Results of the Experiments

B.1. Catalyst Screening

The complete weight change of the samples for alternating CO_2 and H_2, and CO_2 and N_2 can be found in Figures B.1 and B.2. The weight change is normalized for the starting weight of the sample.

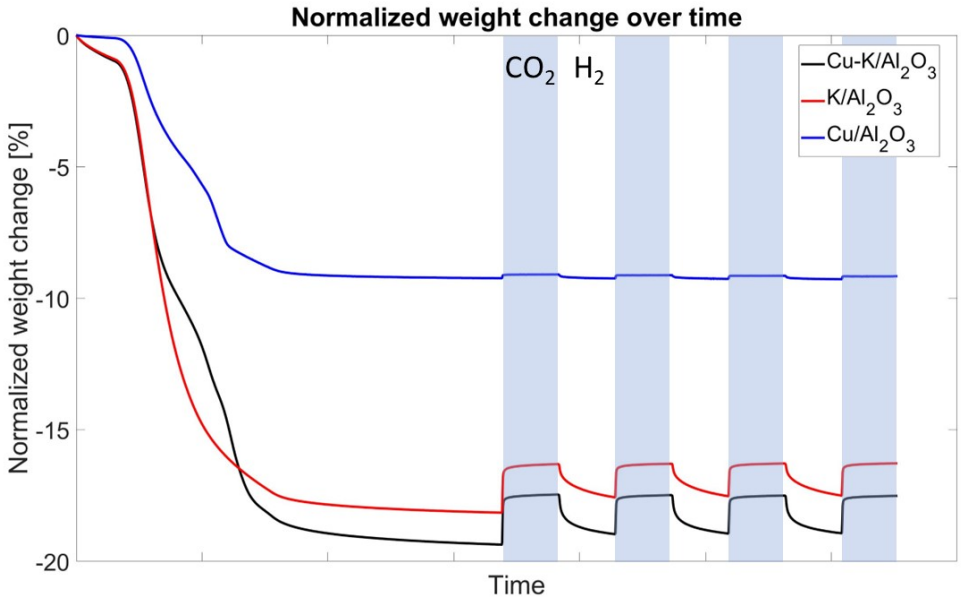

Figure B.1: Weight change as a result of alternating a H_2 and CO_2 flow in the TGA for Cu-K/γ-Al_2O_3 type 1.

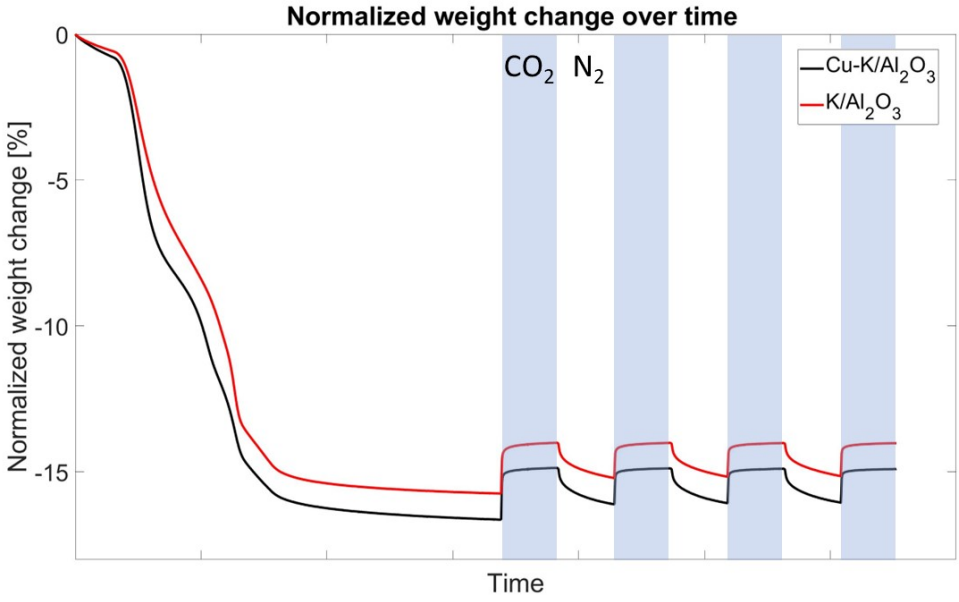

Figure B.2: Weight change as a result of alternating a N_2 and CO_2 flow in the TGA for Cu-K/γ-Al_2O_3 type 1.

B.2. H_2O profiles

In Figure B.3 the H_2O profile for Cu-K/γ-Al_2O_3 type 2 is visualized.

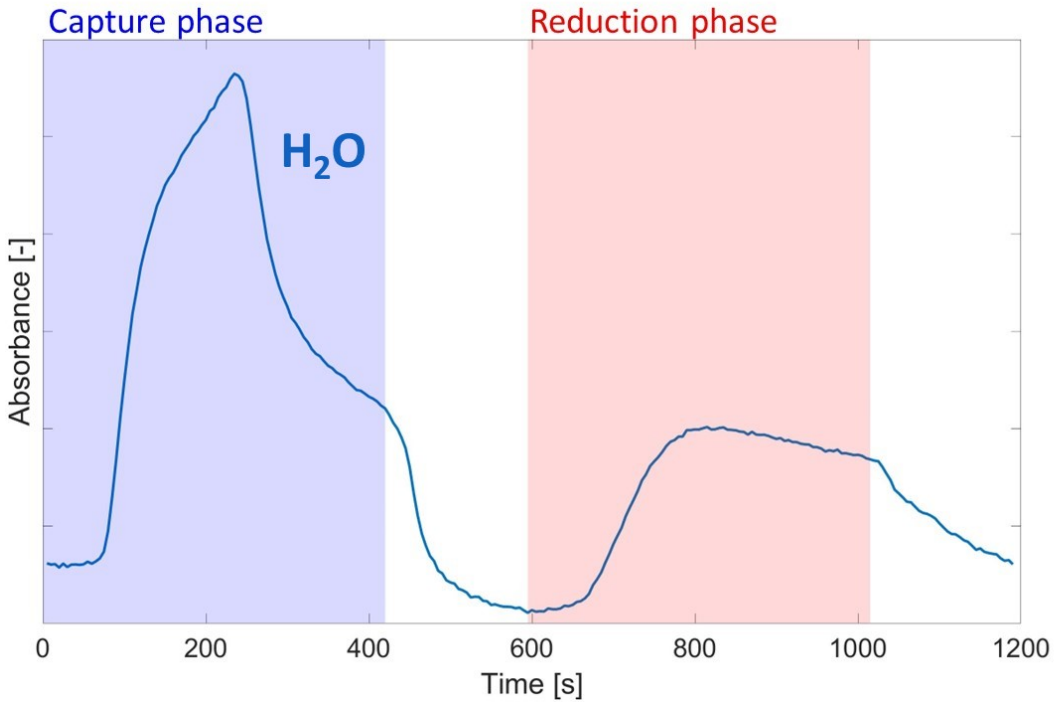

Figure B.3: H_2O profile of 200 mg Cu-K/γ-Al_2O_3 type 2 at 450 °C. During the experiment flows of CO_2 of 15 mL min^{-1}, H_2 of 15 mL min^{-1} and a He-flush of 30 mL min^{-1} are used. The duration of the capture and reduction phase is 420 seconds, the He-flush phase is 175 seconds.

Figure B.4 shows the H_2O profile for Cu-K/γ-Al_2O_3 type 1 and 2 for a short capture and reduction phase duration.

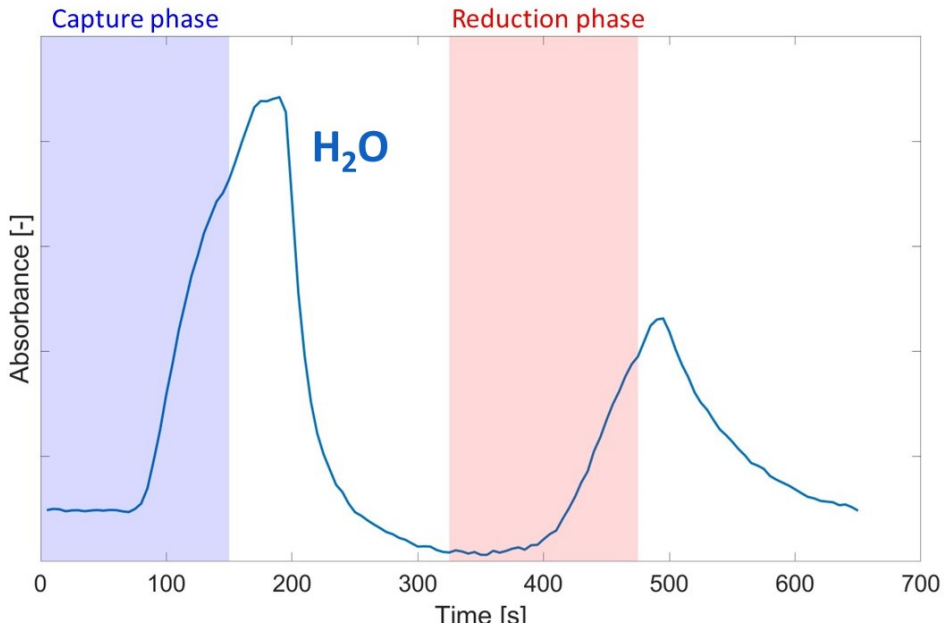

(a) Cu-K/γ-Al_2O_3 type 1.

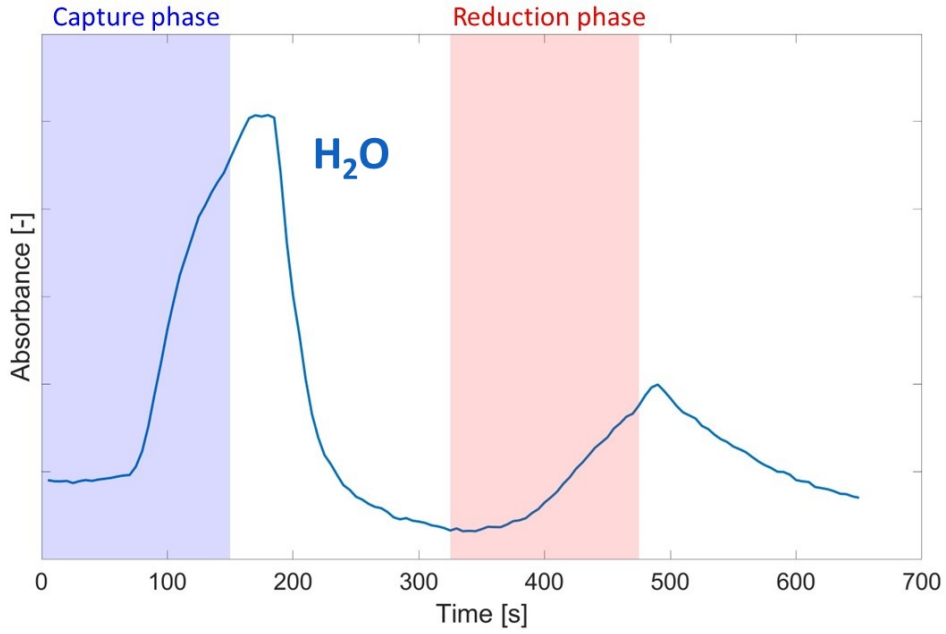

(b) Cu-K/γ-Al_2O_3 type 2.

Figure B.4: H_2O profile of 200 mg Cu-K/γ-Al_2O_3 type 1 (B.4a) and type 2 (B.4b) at 450 °C. During the experiment flows of CO_2 of 15 mL min^{-1}, H_2 of 15 mL min^{-1} and a He-flush of 30 mL min^{-1} are used. The duration of the capture and reduction phase is 150 seconds, the He-flush phase is 175 seconds.

B.3. Full capture

Figure B.5 shows the result of increasing the amount of catalyst. It should be noted that the catalyst bed and particle size has not been optimized for this operation. In Figure B.5a the result is visible for utilizing SiC during the experiment. This demonstrates the CO_2 profile when no catalytic behaviour takes place. Figure B.5b shows that no CO_2 signal is visible in the capture phase. This indicates that all the CO_2 flowing through the reactor is captured by the catalyst. Some CO_2 is visible during the He-flush and the reduction phase, this can be attributed to the not optimized catalyst bed configuration. CO production takes place in the reduction phase. From this experiment it is determined that full CO_2 capture can occur when the process parameters are optimized.

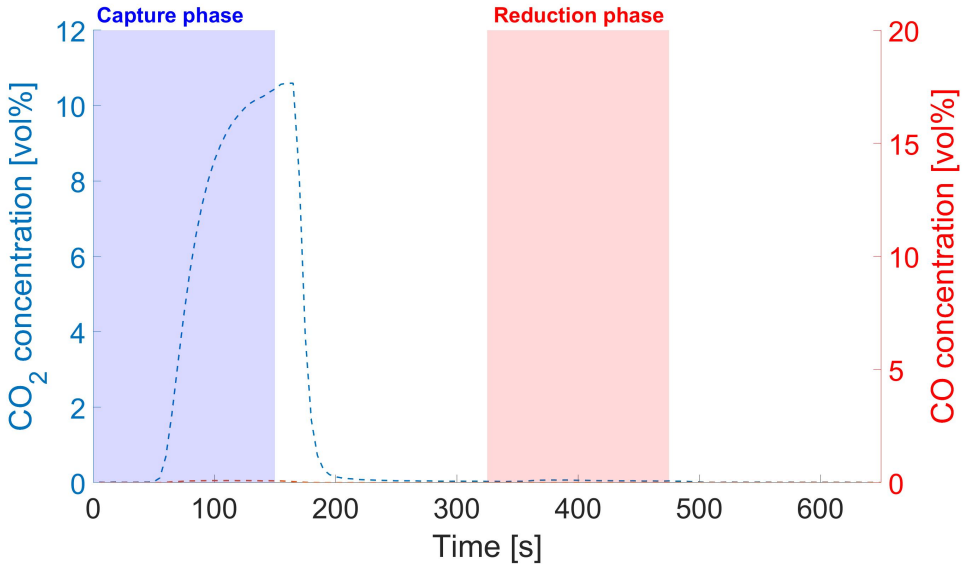

(a) Experiment with SiC

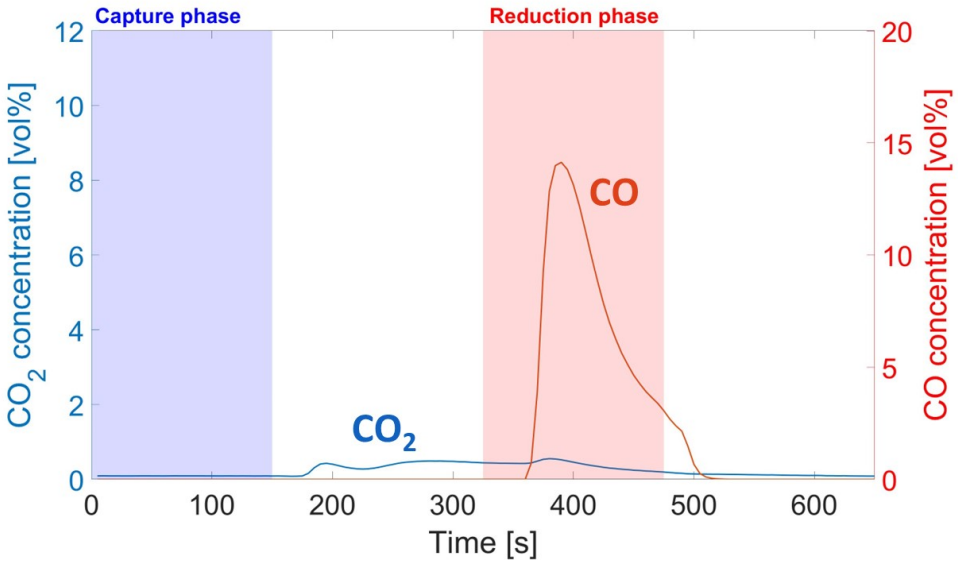

(b) Experiment with Cu-K/γ-Al_2O_3

Figure B.5: Catalytic profile of SiC (B.5a) and 800 mg Cu-K/γ-Al_2O_3 type 1 (B.5b) at 450 °C. During the experiment flows of CO_2 of 10 mL min^{-1}, H_2 of 15 mL min^{-1} and a He-flush of 30 mL min^{-1} are used. The duration of the capture and reduction phase is 150 seconds, the He-flush phase is 175 seconds.

B.4. Calibration curves

Figures B.6 and B.7 show the calibration curves for the H_2 quantification. First, the calibration curve used for the blank measurement is visualized, followed by the calibration curve used for the experiment.

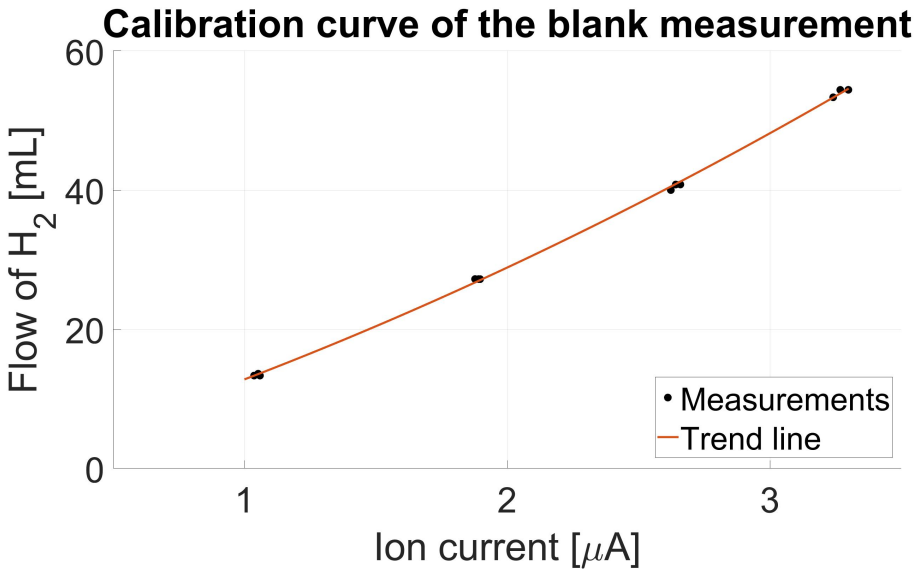

Figure B.6: Calibration curve for blank measurement of Cu-K/γ-Al_2O_3 type 1 catalyst

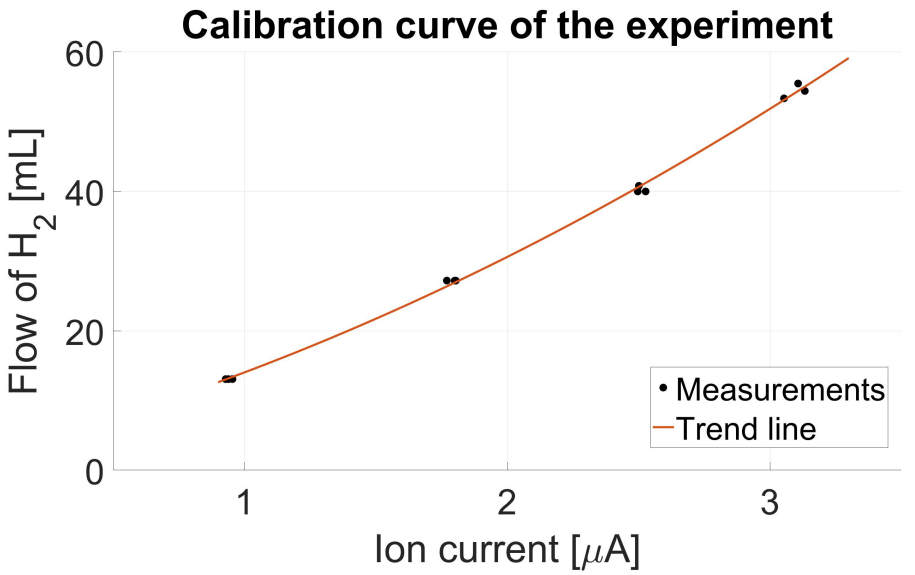

Figure B.7: Calibration curve for experiment of Cu-K/γ-Al_2O_3 type 1 catalyst

C

Catalyst Cost Calculation

To estimate the catalyst cost the approach of Baddour et al. is used [41]. By using a step-based method the production costs for a novel catalyst can be estimated. The inputs into the calculation are the catalyst composition, consumption of raw materials and their price, synthesis steps as well as the amount of catalyst that is produced. In the first base-case scenario it has been assumed that the lifetime of the catalyst is equal to the lifetime of the process. This means that in the catalyst cost calculation it has been assumed that the production size is 11 tonnes. This value is based on the calculations performed in Section 6.1.

In the step method different synthesis steps are mentioned that correspond to the steps performed at lab scale. For each step the costs are mentioned dependent on the scale of the synthesis. In this estimation a medium scale has been utilized based on the amount of catalyst used in this process. The campaign length is 50 hours, taking the cleaning time into account. The hourly production cost can be calculated when utilizing the synthesis steps. During the calculation it has been assumed that the synthesis steps remain equal to the steps taken in the lab. This means twice the cost for the incipient wetness impregnation, for a dryer and for the indirect kiln. This results in an hourly production cost of $750. When multiplying that with the campaign length, the total production cost is determined ($37,800).

Besides the production cost, the cost for raw materials should also be determined. To estimate these costs, the chemicals and their price are used. In Table C.1 the prices can be found.

Table C.1: Cost of raw materials

Material	Cost [€/gr]	Reference
γ-Al_2O_3	0.014	[53]
$Cu(NO_3)_2{\cdot}3\,H_2O_{(aq)}$	0.098	[54]
K_2CO_3	0.01991	[55]

The cost of raw materials for 11 tonnes of catalyst is ±$700. To calculate the overhead costs and a selling margin, the raw materials and synthesis steps costs are first added together. This results in a cost of $3.50 per gram of catalyst. The general and administrative costs are estimated as 5% of this value. The sales, administrative, research, and distribution costs are computed as 5% of the costs of the raw materials, synthesis steps and the general and administrative costs added together.

Based on the size of the order, a selling margin needs to be added to the previously discussed costs. The margin is estimated as 31% of the pre-margin costs ($1.07 per gram of catalyst). This results in a catalyst cost of $4.93 per gram of catalyst. For each reactor the catalyst cost is estimated to be $27,129.